The influence of microstructure on the corrosion behaviour of ferritic-martensitic steel

by

Thomas Remmerswaal

to obtain the degree of Master of Science
at Delft University of Technology,
to be defended on Monday August 24, 2015 at 9:30 PM.

Student number:	4064860	
Project duration:	November 10, 2014 – August 24, 2015	
Thesis committee:	Dr. J. M. C. Mol,	TU Delft, MSE (chairman)
	Dr. M. J. Santofimia Navarro,	TU Delft, MSE (supervisor)
	Dr. Y. Gonzalez-Garcia,	TU Delft, MSE (supervisor)
	Dr. L. Rassaei,	TU Delft, ChemE, OMI

An electronic version of this thesis is available at
http://repository.tudelft.nl/.

TU Delft Delft University of Technology

[This page intentionally left blank]

Acknowledgements

Being a mechanical engineering bachelor graduate, it can be a tedious job to complete a scientific study in the field of metallurgy and corrosion. Therefore, I would like to thank my supervisors for their help during the course of this project.

Many thanks to dr. Yaiza Gonzalez-Garcia for the help with the corrosion experiments. I found out that experiments and results were not always as straightforward as expected beforehand. It has been really helpful to learn to be patient, repeat your experiment and obtain appropriate results.

Thanks to dr. Maria Santofimia Navarro as well for the help designing the microstructures for the different samples. To do this, a structured approach is key, changing one variable a time, which has helped enormously during the dilatometer experiments and characterization of the microstructures.

I would like to thank Agnieszka Kooijman for the help in the labs, especially with the tedious micro-capillary cell. Thanks to dr. Majid Sababi as well for being very good in helping me understand the various key processes in corrosion science.

Finally many thanks to Wilco, Annemarie, Ewout, Danilo and Joep, the flex-room people, for being excellent company during the pauses in between the work on this thesis.

Thomas Remmerswaal, Delft, August 2015

Abstract

Modern steel alloys are composed of several phases, for example ferrite and martensite. By varying the fraction or the size of the grains of these phases, the mechanical properties of the alloy can be altered. These microstructural variations were already found before to influence the corrosion properties of the alloy; this has been investigated in this master thesis by means of electrochemical experiments. The prior austenite grain size has been varied for fully martensitic samples; it was found that grain boundaries are less noble sites in the lattice and that an increase in prior austenite grain boundary density would increase the corrosion rate. Grain boundaries were found to be anodic initiation sites for pits. However, since fine microstructures have more initiation sites, fewer pits would grow critical due to the lack of compensating cathode area. The depth and size of the pits in the fine-grained material were found to be larger than those in the coarse-grained samples.

When the amount of ferrite in the ferritic-martensitic samples was increased, the corrosion potential became more negative. The ferrite formed a galvanic couple with the martensite and corroded preferentially due to its lower (more negative) corrosion potential. The corrosion current density was found to peak at a certain ferrite fraction. However, the anodic dissolution rate of the ferrite was found to decrease with increasing ferrite fractions, since the cathode-to-anode area ratio became less favourable for galvanic corrosion. The nucleation of ferrite also partitioned more alloying elements to the austenite, during annealing, due to the higher solubility of those elements in austenite. The alloying elements were found to sacrificially corrode for the iron, forming a protective layer of reaction products on the martensite surface. The corrosion potential for the martensite was found to increase with increasing amounts of alloying elements, while the current density decreased and the corrosion rate was retarded. These changing electrochemical properties of the martensite also influenced the corrosion properties of the ferritic-martensitic alloy on the macroscopic scale.

Reading guide

This report is built up as follows: first the topic will be introduced, explaining briefly the theory behind metallurgy and corrosion. After that, in Chapter 2, the experimental procedure is explained: the material that was tested is described, including the heat treatments that were performed. The techniques that were used to obtain results about the corrosion behaviour of the samples are explained as well. The results of both the microstructure making as the corrosion experiments will be explained in Chapter 3, together with the discussion on these results. Chapter 4 contains the drawn conclusions from the experiments and Chapter 5 displays the recommendations for future research.

Nomenclature

(A)	Concentration of element A [-]
α	Ferrite phase in iron
α'	Martensite phase in iron
α_{TH}	Thermal expansion coefficient [K^{-1}]
ΔG	Gibbs free energy change [J/mol]
ΔG_0	Standard Gibbs free energy change [J/mol]
δ	High temperature BCC iron phase
γ	Austenite phase in iron
a	Molar mass [g/mol]
D	Density [g/cm^3]
E	Corrosion potential [V vs SHE]
e_0	Standard potential [V vs SHE]
E_A	Activation energy [J/mol]
e_a	Anodic electrode potential [V vs SHE]
e_c	Cathodic electrode potential [V vs SHE]
F	Faraday constant: 96,500 [C/mol]
f_α	Ferrite fraction [-]
f_γ	Austenite fraction [-]

f_F	Ferrite fraction [-]
f_M	Martensite fraction [-]
I	Corrosion current [A]
i	Current density [$\mu A/cm^2$]
M_s	Martensite start temperature [K] or [°C]
n	Amount of exchanged electrons
R	Universal gas constant: 8.314 [J/mol K]
S_c	Anode area fraction [-]
S_c	Cathode area fraction [-]
S_{sample}	Sample area [cm^2]
T	Temperature [K] or [°C]
A1-temperature	Eutectoid temperature [K] or [°C]
A3-temperature	Austenite solidus temperature [K] or [°C]
at%	atom percent
BCC	Body-Centered Cubic crystal structure
BCT	Body-Centered Tetragonal crystal structure
CR	Corrosion rate [cm/s]
FCC	Face-Centered Cubic crystal structure
OCP	Open Circuit Potential [V vs SHE]
PAGS	Prior Austenite Grain Size
SEM	Scanning Electron Microscope
SHE	Standard Hydrogen Electrochemical potential [0.0V vs SHE]
wt%	weight percent
XRF	X-Ray Fluorescence Spectroscopy

Contents

List of Figures

List of Tables

Chapter 1

Introduction

1.1 Metallurgy

Metallurgy is based on the minimization of the Gibbs free energy of the material by the material itself. Metals, with few exceptions such as mercury, are crystalline solids at room temperature which tend to arrange its atoms in an ordered manner. This means that, on a sub-micron scale, the structure is reproducible with the smallest reproducing feature being the unit cell [10]. For the equilibrium phases in iron, the two crystal structures are Body Centered Cubic (BCC), at low temperatures, and Face Centered Cubic (FCC) at higher temperatures in between roughly 700 and 1400°C. Above this 1400°C, another BCC phase will become stable. Both the unit cells of the BCC and FCC crystal structures are shown in Figure 1.1.

At room temperature, iron has a BCC crystal structure. However, steel is not composed of iron alone, but carbon is (amongst others) present in the iron matrix as well. Carbon has a lower atom number in the periodic table, which means that the atom consists of a smaller core and fewer electrons in its shell. Smaller atoms, such as carbon, can occupy the volume that is in between the atoms of the crystal lattice. For the BCC crystal structure, there are four places (tetrahedral sites) in one unit cell to accommodate these so-called interstitials, such as carbon, while FCC can contain eight interstitials per unit cell (on the octahedral sites). Since FCC can contain more interstitials per unit cell, the solubility of carbon (interstitials) in FCC is generally higher than in BCC, which is seen hereafter in the phase diagram.

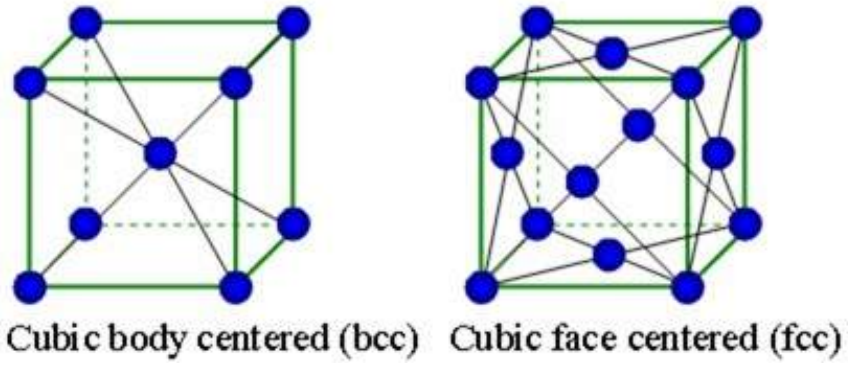

Figure 1.1: Crystal structures of iron [1].

1.1.1 Phase diagram

The stable phases of steel were found to vary with temperature and concentration of alloying elements, such as carbon. In a phase diagram, of which an example is shown in Figure 1.2, the stable phases are displayed as a function of both these variables. Figure 1.2 displays an iron-carbon phase diagram, which is used most often as a simplification for the phase diagram of (low-alloyed) steel phase diagrams. It can be seen that, for very low carbon concentrations and temperatures in between 400 and 900°C, the iron is present as BCC ferrite. For higher carbon contents, the ferrite is stable until the A1-temperature, which is 727°C in this case. Cementite, an iron-carbide (Fe_3C) will be present in the ferrite when the carbon content is higher (to the right of the right boundary of the ferrite phase) than the equilibrium content.

When the temperature is increased above the A1-temperature, FCC austenite will start to form. In Figure 1.2, a region can be seen in which α and γ (ferrite and austenite) are present. Both phases will then be present in equilibrium in this so-called intercritical region. The highest possible temperature in the intercritical region is the A3-temperature; above this, only austenite will remain stable and all ferrite would have been dissolved. For higher carbon contents, at least above 2.14wt% (depending of temperature), austenite will be in equilibrium with cementite.

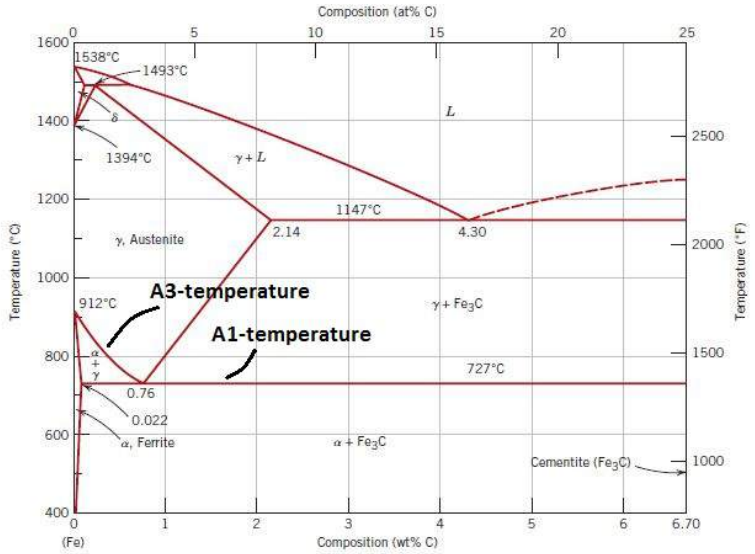

Figure 1.2: Iron-carbon phase diagram, showing the stable phases for certain compositions (carbon content) and temperatures [2].

1.1.2 Phase transformations

When the steel is cooled from the γ- towards the α-phase, this new ferrite phase needs to nucleate in the austenite before it can grow. For the nucleation, a certain amount of undercooling below the equilibrium temperature is needed, because otherwise no driving force for nucleation is present. The growth of new amounts of phase is time-dependent, since nucleation is a probabilistic process and growth is not instantaneous. This means that by changing the cooling rate, the resulting microstructure can be altered. Nucleation of ferrite will generally happen at the austenite grain boundaries and triple points, because the energy level is higher at those places as compared to the bulk material; the high energy level will lower the activation energy (E_A) for nucleation. Diffusion of alloying elements, such as carbon, will play a role during the growth of the new phase throughout the sample. The equilibrium carbon content (and that of other elements) in the intercritical region is lower for ferrite as compared to austenite. Therefore, after the nucleation of ferrite, the excess of carbon needs to diffuse away, in front of the freshly formed ferrite. Diffusion times are long enough when the cooling rate is very low and equilibrium behaviour according to the phase diagram can be expected. However, when the cooling rate is increased, excess carbon

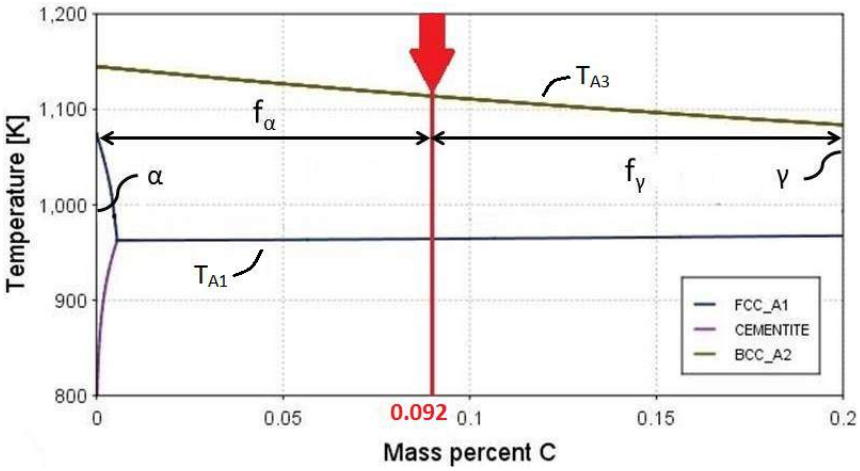

Figure 1.3: Iron-carbon phase diagram, red line displays carbon content along which cooling takes place.

can be frozen in the matrix since the diffusivity will decrease rapidly with temperature and diffusion times will shorten.

Figure 1.3 displays the cooling trajectory through the intercritical regime in an iron-carbon phase diagram. The red line displays the carbon content of the alloy that was used in this work (0.092wt%). When the sample is cooled from the austenite region to a temperature in the intercritical regime, the phase separation causes the microstructure to have a fraction (f_α) of ferrite and a fraction of austenite (f_γ). It can be seen that the values of these fractions will vary as the annealing temperature is varied since the distances towards the boundaries of the ferrite (on the left) and the austenite (on the right) will change, according to the lever rule [11].

1.1.3 Martensite

When the austenite is rapidly cooled or quenched below a certain temperature (martensite start temperature; M_s), martensite will form. When the austenite is quenched, there is not sufficient time to move away the excess carbon in front of the $\gamma - \alpha$-interface. This will cause the matrix to be supersaturated with carbon, resulting in a BCT crystal structure. BCT is similar to BCC, but has the lattice parameter stretched in one direction to accommodate a higher amount of interstitial carbon atoms per unit cell. The stretched lattice, compared to the equilibrium ferrite microstructure,

will impose a very high strength, but also a low ductility, which causes the martensite to behave very brittle. The martensite start temperature (M_s) is a function of the chemical composition of the alloy, as can be seen in Equation (1.1), in which the X's represent the weight percentage of that specific element [12, 13].

$$M_s(^\circ C) = 539 - 423X_C - 30.4X_{Mn} - 12.1X_{Cr} - 17.7X_{Ni} - 7.5X_{Mo} + 10X_{Co} - 7.5X_{Si} \tag{1.1}$$

When martensite forms, its crystal structure is complex. Martensite grains are not homogeneous, but are built (in order from small to large) out of laths, blocks and packets, which can be seen in Figure 1.4. The largest features are the prior austenite grains, which are defined as the regions that made up one austenite grain at the normalizing or annealing temperature. Laths are the smallest features in the martensite microstructure and are the actual individual grains. Blocks are arranged as a collection of laths with similar crystallographic orientation. Packets are formed out of several blocks, that had the same {111} plane in austenite. Finally, different packets can appear since four different {111} planes are present in the austenite, as they share the same family of planes [3, 14]. Prior austenite grain remain visible, since nucleation of martensite started in the prior austenite grain boundaries. This causes the fact that no martensite grains will continue through the prior austenite grain boundary.

One last remark is that, in practice, not all austenite is transformed into martensite. The remaining (not yet transformed) austenite can be retained if carbon diffuses into it from the martensite. In practice, diffusion can happen when quenching rates are not high enough. The excess carbon will stabilise the austenite, so it can stay present at room temperature, which is caused by the lowering of the martensite start temperature. For the scope of this research, however, it is assumed that quenching rates are high enough, and alloying elements concentration low enough, to prevent the formation of retained austenite [13].

Boundaries in martensite

The mentioned laths, blocks, packet and prior austenite grains all have boundaries in between them. The nature of these boundaries is different, each type having a certain energy level. The boundaries between laths, the smallest features, mostly are low-angle boundaries [13]. Low angle means that the misorientation of crystal direction between both laths is small.

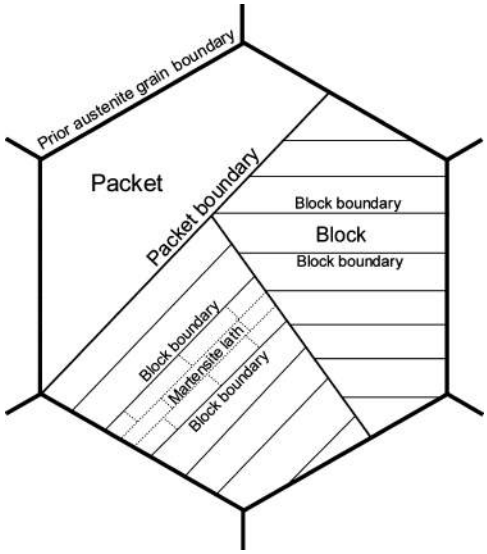

Figure 1.4: Microstructure of martensite showing a prior austenite grain with, packets, blocks and laths [3].

The mentioned {111} habit plane could occur in 4 different families of planes. This means that, at most, 4 different principal {111} directions can be formed, found in so-called packets. The packet boundaries will be coherent since they share the same family of habit planes [15]. Coherent boundaries will have a lower energy level as compared to incoherent boundaries, since the atoms in both grains will be closer to each-other, with few misfits [11], so it has many resemblances with a normal crystal. Blocks are, finally, composed of martensite laths which had different variants, but had the same {111} planes. The prior austenite grain boundaries, the largest considered features, will be incoherent thus having the highest energy level.

For alloys with high carbon contents, above 1.4wt%, twin boundaries could form between the laths [13, 15]. In a twin boundary, the structure on each side of it will be a mirror image of the other side. These type of boundaries will have a very low energy level, but will also be the weakest barriers during deformation (dislocation movement).

Martensite in commercial steels

The main property of martensite, being very strong, is commonly used in the steel-making industry. However, the lack of deformability, due to the high

internal stresses, causes commercial alloys never to be fully martensitic. An alloy that is consisting of martensite and other phases is the best alternative. A relatively old alloy (from the 1960's) is the ferrite-martensite dual-phase alloy, in which the martensite induces strength, while the sliding mechanism between martensite and ferrite induces great deformability. Generally, these dual-phase alloys are composed of around 80% ferrite and 20% martensite. The retained austenite that can be present between the martensite regions is used as well in other alloys, for example in Quenching and Partitioning (Q&P) steels and TRansformation Induced Plasticity (TRIP) steels. The displacive Kurdjumov-Sachs transformation from austenite to martensite is used in the application when a stress in the $\langle 111 \rangle$-direction will initiate the martensitic BCT crystal structure in the retained austenite.

1.2 Corrosion theory

Corrosion is defined as the destructive result of the reaction between a metal (alloy) and its environment [4]. In nature, these metal alloys are usually present as minerals, for example as oxides or silicates. During the production of the metal alloy, energy is brought into the mineral to purify it into elemental form. During the corrosion process, the metal degrades electrochemically, forming the mineral (metal-oxide) again.

1.2.1 Electrochemistry

The mechanism behind a corrosion reaction is based on the transfer of electrons. When a chemical reaction is based on the transfer of electrons, this reaction is called an electrochemical reaction. During a corrosion reaction, metals are oxidized, while other species (generally non-metals) reduce, consuming the produced electrons from the oxidation process.

The corrosion reaction is always based on two half-cell reactions, one by which electrons are produced and one by which electrons are consumed. When a metal is corroded, this will result in the dissolution of the metal atoms, forming (charged) ions and electrons, as can be seen in Equation (1.2).

$$M \rightarrow M^{n+} + ne^{-} \tag{1.2}$$

Oxidation of this metal atom will require a certain amount of energy, since the metal atom is at the lowest possible energy state. This energy difference will be, through the Faraday constant, associated with an electrochemical

potential ($\Delta G = -n * F * E$). The electrochemical reaction that produces electrons is called the anodic or oxidation reaction, having an electrode potential e_a.

For the reaction that consumes the electrons, the cathodic reaction, the charge transfer introduces an energy difference between the ionized state and the final state. Since both anodic and cathodic reactions occur at the same time, the sum of both energy differences is the total amount of energy that is transferred during the reaction.

The electrochemical potential cannot be measured as an absolute value, since there is no fixed reference state. Therefore, the potential of the hydrogen reduction reaction, Reaction (1.3), is defined at 0.0 Volt. This means that, for all other possible electrochemical reactions, a potential difference can be measured with respect to this reference.

$$H_2 \rightleftharpoons 2H^+ + 2e^- \tag{1.3}$$

Influence of environment on corrosion

The electrode potential, by definition, has a certain value in a defined standard environment. This means that when the environment changes, the potential is likely to change as well. It is obvious that when the amount of reactant is decreased, the potential and energy difference of the reaction will change. Suppose, an electrochemical reaction will happen as in Equation (1.4), with a and b being the number of reacting atoms of respectively species A and B.

$$a \times A + m \times H^+ + n \times e^- \rightarrow b \times B + d \times H_2O \tag{1.4}$$

When the environment changes and the concentration of reaction products and reactants changes, the associated energy will change as well, as can be seen in Equation (1.5).

$$\Delta G = \Delta G^0 + RTln\frac{(B)^b(H_2O)^d}{(A)^a(H^+)^m} \tag{1.5}$$

The terms between parentheses are the concentrations of the reaction products and reactants. The influence of concentration will result in the fact that a material never has a fixed corrosion potential, but that this potential should always be defined with respect to a reference and with a description

of the environment. From the change in Gibbs free energy, the potential can be derived by dividing the change in energy by the amount of exchanged electrons and the Faraday constant ($F = 96,500 C/mol$). Equation (1.6) displays this electrode potential in the so-called Nernst equation.

$$e = e_0 + \frac{RT}{nF} ln \frac{(B)^b (H_2O)^d}{(A)^a (H^+)^m} \tag{1.6}$$

Equation (1.6) also shows the effect of hydrogen (ions) concentration. A solution with high hydrogen concentration is also called acidic, with pH ($pH = -log([H^+])$) being the unit that describes acidity. The acid influences the corrosion properties of the material. Figure 1.5 shows a so-called Pourbaix diagram, which explains the state of the sample, given the pH and electrode potential, and explains whether the material is expected to corrode or not, based on the stability of the phases. The dashed lines in the Pourbaix diagram are lines obtained using equations like Equation (1.6), in which the electrode potential is calculated as function of concentration of hydrogen ions. The different stable states of the iron are *corroding*, *immune* and *passive*. Corroding (also called active) means that the metal will oxidise, while in the immune state, the iron cannot corrode. When the iron is passivated, a protective oxide layer is present on the surface which will prevent the iron from coming into contact with the environment and therefore slows down the reaction.

pH, on the x-axis of the Pourbaix diagram, is generally a given property in the system. However, it can also change when corrosion takes place due to consumption or production of H^+-ions. The electrode potential, which is displayed on the y-axis of the Pourbaix diagram, can be varied during experiments. During this variation, it is therefore possible to change the state of the material and change the behaviour of the metal from active towards passive or immune.

Electrolyte

Charge transfer from anode to cathode needs to be accommodated to allow for a corrosion reaction to happen. On the first hand, the electrons need to be able to flow from anode towards the cathode. Since anode and cathode are generally both located on the metal surface, electrical conduction forms no barrier. The dissolved ions also need to be transported away, which means that a layer of liquid needs to be present on the sample surface. This conducting liquid, also called electrolyte, must be able to dissolve the ions

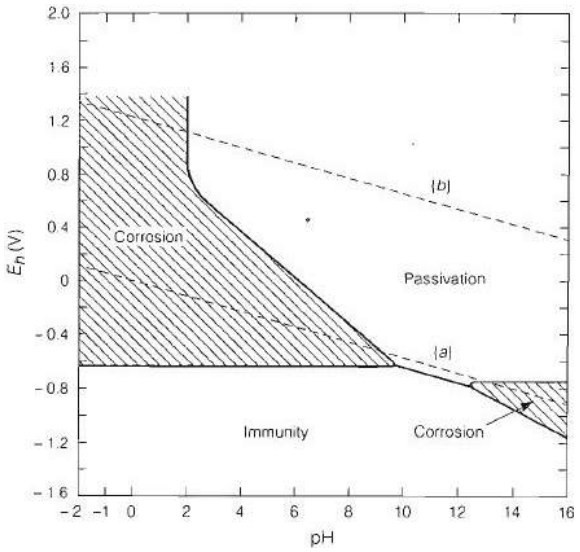

Figure 1.5: Pourbaix diagram for iron, showing the stable phases of the iron as function of pH (hydrogen ions concentration) and electrode potential [4].

that are produced at the anode. On the other hand, the electrolyte also needs to supply the to-be-reduced species towards the cathode.

The corrosion reaction will be influenced by the electrolyte. It has already been seen in the Pourbaix diagram that when the hydrogen concentration in the electrolyte (pH) is altered, the stable phases of the to-be-corroded material can be altered. An electrolyte that is rich in ions will also be able to conduct the charged ions better. Finally, dissolved species, such as chlorine ions, can influence the corrosion reaction.

Kinetics and corrosion rate

The charge transfer, caused by the production and consumption of electrons at the anode and cathode respectively, will result in an electric current. The current represents the charge (in Coulombs) that is transferred per unit of time (seconds). The corrosion rate can be calculated using Faradays law [4], knowing the mentioned current, as can be seen in Equation (1.7).

$$CR = \frac{i \times a}{n \times F \times D} \tag{1.7}$$

In Equation (1.7), i is the current density, a the molar mass, n the amount of exchanged electrons, F the Faraday constant and D the sample density.

The potential difference between both half-cell reactions will determine the free energy change of the reaction. However, the potential difference does not give any insight in the kinetics of the reaction, since otherwise the rate would be unlimited when there is a potential difference present. The supply of reactants will be influencing the kinetics, since the reaction rate decreases when there is a reactants deficit.

1.2.2 Corrosion of iron

When iron (or steel) is corroding, the oxidation reaction as in Equation (1.8) will occur.

$$Fe(s) \rightarrow Fe^{2+} + 2e^{-} \tag{1.8}$$

It can be seen that solid iron atoms will dissociate, producing positively charged ions and 2 electrons. At the cathode, depending whether dissolved oxygen is present in the electrolyte, the reduction reaction as in Equation (1.9) or (1.10) will occur.

$$O_2 + 2H_2O + 4e^{-} \rightarrow 4OH^{-} \tag{1.9}$$

$$2H_2O + 2e^{-} \rightarrow H_2(g) + 2OH^{-} \tag{1.10}$$

For Reaction (1.9) to occur, dissolved oxygen is needed, while for Reaction (1.10) only water molecules are needed. When the electrolyte is in contact with air, a balance will occur between the oxygen in the air and the dissolved oxygen in the electrolyte. Figure 1.6 shows the corrosion process for iron in water schematically. It can be seen that iron will dissolve, according to Reaction (1.8), at the anode. At the cathode, oxygen will react with water to form hydroxyl ions (according to Reaction (1.9)).

Table 1.1 displays the mentioned half-cell reactions. Note that the potentials of the reactions in this table are standard potentials, meaning that they are obtained for an aqueous solution at 25°C (under standard conditions). The final electrode potential of these reactions will be changed by the electrolyte and the concentration of dissolved species. For Reactions (1.9) and (1.10), the pH of the solution is taken as 14, representing a very alkaline (non-acid) solution. Since hydroxyl-ions are a reaction product, both

Reaction	Potential (V) vs SHE
$Fe(s) \rightarrow Fe^{2+} + 2e^-$	-0.447
$O_2 + 2H_2O + 4e^- \rightarrow 4OH^-$	+0.401 ($pH = 14$)
$2H_2O + 2e^- \rightarrow H_2(g) + 2OH^-$	-0.828 ($pH = 14$)
$2H^+ + 2e^- \rightarrow H_2(g)$	0.000

Table 1.1: Standard corrosion potential for corrosion half-reactions under standard condition (25°C, aqueous solution) versus Standard Hydrogen Electrode (SHE)[7, 8]

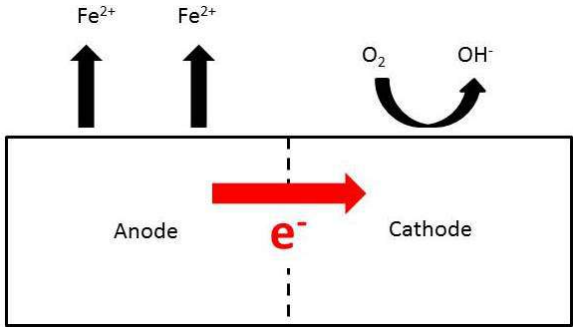

Figure 1.6: Scheme of corroding iron surface, with the anode at which iron dissolves and the cathode on which the oxygen evolution reaction takes place.

reaction balances would be shifted to the right if the solutions were not to be fully saturated with hydroxyl-ions. Note that, using the Nernst-equation (as in Equation (1.6), the corresponding potentials for a neutral (pH=7) solution can be calculated. These are found to be $+0.82V$ for Reaction (1.9) and $-0.413V$ for Reaction (1.10).

1.2.3 Types of corrosion

It has been seen that corrosion is based on the exchange of charge and matter between an anode and a cathode. Material, geometry and environment of the sample will influence the corrosion process as well. Below, several types of corrosion are explained.

General corrosion

The most common corrosion type is global corrosion. When global corrosion takes place, the iron will be oxidized globally across the entire sample surface. A general feature of global corrosion is the presence of a brown layer on the surface, after the sample has been corroded. This layer is formed of reaction products caused by the iron ions that reacted with hydroxyl ions, as in Reaction (1.11), forming (passive) iron-hydroxide.

$$Fe^{2+} + 2OH^- \rightarrow Fe(OH)_2 \tag{1.11}$$

Global corrosion is the least dangerous of all corrosion types or at least the most predictable, since its presence can be detected well and the attack is over the entire surface, meaning that the inward penetration is small.

Galvanic corrosion

It has been seen that half-cell reactions possess a certain electrode potential. This potential is not the same for every material; copper for example will have a standard potential of +0.342 Volt, compared to the -0.477 Volt for iron. When both metals are coupled, a corrosion reaction between both can happen as a result of this potential difference. The least noble metal, being the one with the lowest electrode potential (compared to the reference state) will corrode, while the more noble one will remain intact and will facilitate the cathodic reaction. This effect of two coupled metals is often called the galvanic effect [16].

Area ratio When the cathode over anode area ratio is taken large, the cathode area is large compared to the anode area. This means that the reduction reaction takes place on a large surface, so the diffusion of species towards it becomes less limiting. Equation (1.12) shows the ratio between anodic and cathodic current density as a result of the area of both.

$$I_{\text{galvanic couple}} = I_a = I_c \rightarrow i_a \times S_a = i_c \times S_c \rightarrow \frac{i_a}{i_c} = \frac{S_c}{S_a} \tag{1.12}$$

When the cathode over anode area ratio is large, the anodic dissolution rate (i_a) becomes large as well, resulting is the most damage on the sample.

An example of this area effect is shown in Figure 1.7. The left part of the figure shows a small cathode (C), next to a large anode. The limited diffusive supply of oxygen towards the cathode will retard the reaction, lowering the

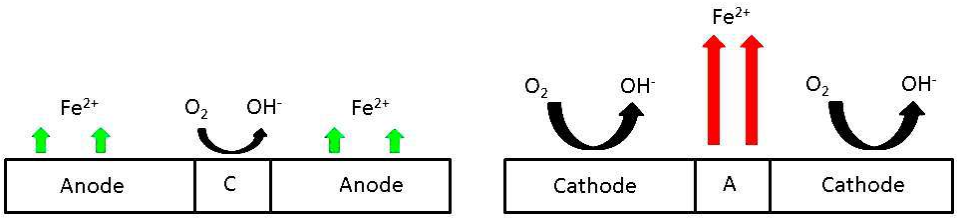

Figure 1.7: Galvanic corrosion with favourable (left) and unfavourable (right) area ratio, showing favourable (green) and unfavourable (red) iron dissolution

corrosion rate. The right part of the image shows a large cathode, compared to a small anode (A). Diffusive supply of oxygen no longer forms a problem, so the overall dissolution rate of iron is much higher.

Localized corrosion, pitting

It has been seen in the Pourbaix diagram that a metal can become passive, provided that the pH and electrode potential are in the right range. In the passive state, an iron-oxide (Fe_2O_3) layer on the surface will block the reaction, since it prevents the iron from coming into contact with the environment. Damages in the passive layer can always be present, for example by a scratch or dent that was introduced on the surface. Locally, the passive layer will be broken as a result, exposing the iron again. This active iron will be reactive and has a lower corrosion potential as compared to the surrounding passive layer [4]. Between the active iron and the passive layer, a galvanic couple can form, as can be seen in Figure 1.8. The passive layer facilitates the cathodic reaction and iron is dissolving in the anodic pit. The danger of this process is the localized presence of pits. Since the holes in the passive layer are small, it is hard to observe the pits visually. Besides that, caused by the positively charged iron ions, pits have the tendency to expand underneath the iron-oxide surface.

In the pit, iron is dissolving, introducing a positive charge in the pit. Most corrosion tests are performed in seawater, which mainly consists of water with dissolved sodium-chloride. The chlorine ions in the water or electrolyte are negatively charged and are thus attracted by the positively charged iron ions. Chlorine ions are known to destabilize the passive layer of the steel and increase corrosion rates in the pit [17]. This is caused by

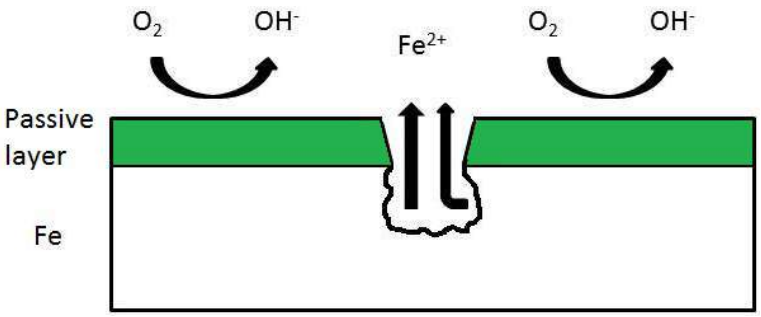

Figure 1.8: Scheme of a corroding pit, showing the passive iron-oxide layer and the active pit with dissolving iron.

the reaction mechanism that is changed, as can be seen in Reaction (1.13).

$$Fe^{2+} + 2H_2O + 2Cl^- \rightarrow Fe(OH)_2 + 2HCl \tag{1.13}$$

The chlorine will attach to the hydrogen ions, forming hydrochloric acid. This acid will increase the anodic dissolution rate even more, as it makes the iron more active. The increased amount of produced iron ions, in the end, will increase the chlorine content in the pit and enhance the corrosion rate even more [4].

1.3 State-of-the-art

In multi-phase steels, local differences in microstructure, such as phase fractions, morphology and compositions can give rise to different corrosion properties. It has been found before [18, 19, 20] that two dissimilar phase morphologies are able to generate a galvanic couple. Previous research has found an influence of microstructure (grain size, composition) on corrosion properties of steel already. Below, the previous work is summarized, specifically looking to the influence of grain size, phase fraction and local composition.

1.3.1 Influence of grain size

Ralston and Birbilis [21, 22] have found that for several metals, a finer microstructure gives rise to a more reactive surface. This means that smaller grains, hence: more grain boundaries, will make the sample more prone to corrosion. It must be noted that this result has been found for active surfaces (assumed when current densities are above $10\mu A/cm^2$), while passive surfaces have not shown any effect. Since grain boundaries have a higher

energy level, due to incoherencies between both neighbouring grains, they will be more reactive as compared to the base material.

Pitting behaviour has also been found to be influenced by grain size. Bhagavathi *et al.* has found that a finer microstructure shows less pitting after 120 hours of submersion in 3.5wt% NaCl solution [19]. With less pitting, it is meant that fewer pits are observed on the corroded surface; nothing has been mentioned about the depth of the pits.

Ramirez *et al.* have found for stainless steels that pits will initiate at grain boundaries and defects in the microstructure, such as precipitates [23]. This mechanism is again based on the higher energy level at those places, forming preferential sites for pits to initiate. This also means that a finer microstructure will result in more initiated pits. Marcus *et al.* have found that the oxide layer of a fine-grained base metal alloy is fine-grained as well [24]. It has been found that the grain boundaries in the oxide layer form favourable diffusion paths for ions between the environment and the metal/oxide interface. Pit initiation is favourable at those boundaries, since the rate of iron dissolution will be the highest there. This assumption however opposes the previous results of Bhagavathi *et al.*[19].

No previous research has been found to be done on the corrosion properties of martensite. However, considering the influence of grain size on corrosion properties for other materials, it can be assumed that a study towards the corrosion behaviour of martensitic steels can be useful.

1.3.2 Influence of phase fraction

The phase fractions in multi-phase materials have been found to influence the corrosion properties. Qu *et al.* have found for low-alloy carbon steels that the corrosion potential for a coupled ferrite-bainite microstructure is lower, compared to the potential for a sample with ferrite alone [18]. This test has been performed in 3.5wt% NaCl solution and also shows the preferential corrosion of ferrite. This means that the ferrite and bainite form a galvanic couple of which bainite is the most noble phase. An optical examination has shown that the thickness reduction (material loss) is larger for ferrite and the corrosion seems to start in the ferrite as well.

Bhagavathi *et al.* have found a difference in the corrosion properties between a ferritic-martensitic and a ferritic-pearlitic microstructure [19]. It has

been observed that the galvanic effect is not as big for the ferritic-martensitic microstructure as compared to the ferritic-pearlitic microstructure. The microstructural differences between ferrite and martensite are also less, which probably explains the decreased galvanic effect. The BCC crystal structure for ferrite is similar to the BCT crystal structure of martensite. The carbon content is different between ferrite and pearlite or martensite, giving rise to microstructural differences between both.

Increasing the amount of martensite up to 50% in a ferritic-martensitic microstructure has been found to increase the current density [20, 25]. Both these experiments were performed on low-alloyed carbon steels with concrete and 3.5wt% NaCl surroundings respectively. Keleştemur has also found that the active region, the region in which the steel will corrode, will be larger when more martensite is added into the microstructure. At some point, no passivation will occur, since the active region has grown above the pitting potential (the potential at which the passive layer starts breaking down).

1.3.3 Influence of local composition

The local composition has been found to influence the corrosion rate of the sample. What is meant with local composition, is a difference in composition of alloying elements between the different phase morphologies. In the earlier-mentioned work of Bhagavathi [19], it has been found that the galvanic effect increases when the two occurring phase morphologies are more dissimilar, both in crystal structure as in composition. The extra alloying elements will increase the corrosion potential of the martensite. This increase in corrosion potential will make the martensite more noble and increases the potential difference between the martensite and ferrite.

The same effect has been mentioned by Revie *et al.* [26]: the corrosion potential increases to higher values with respect to the reference state when more alloying elements are present, making the alloy more noble. This increased protection against corrosion is caused by the layer of reaction products on the surface during corrosion. Most of the typical alloying elements in steel (except for nickel) are less noble than the iron matrix, which is shown in Table 1.2. Note that the electrode potentials mentioned here are again standard potentials, without taking the concentration of elements in the electrolyte into account. The less noble alloying elements (compared to the iron matrix) will sacrificially dissolve for the iron during the polarization of the sample and the reaction products settle as a layer on the surface

Reaction	Potential (V) vs SHE
$Fe(s) \rightarrow Fe^{2+} + 2e^-$	-0.447
$Mn(s) \rightarrow Mn^{2+} + 2e^-$	-1.18
$Cr(s) \rightarrow Cr^{3+} + 3e^-$	-0.744
$Al(s) \rightarrow Al^{3+} + 3e^-$	-1.662
$Ni(s) \rightarrow Ni^{2+} + 2e^-$	-0.257

Table 1.2: Electrode potential for corrosion half-reactions of metallic alloying elements in steel under standard conditions [9]

[27]. This surface layer will then become more protective compared to the iron-only case since it will limit diffusion from the electrolyte to the metal surface. This extra protection will therefore make the alloy more noble and limit the anodic dissolution of the iron, meaning the corrosion rate is lowered. Nickel, mentioned to be more noble than the iron, is expected to decrease the anodic activity of the matrix in which it is dissolved.

1.4 Approach

In previous research, the influences of grain size, phase fraction and local composition on corrosion properties have been investigated, but not fully independent of each other. The overall composition of the alloy, for example, has also been altered in previous research. This causes some results and conclusions to be dependent of multiple microstructural features. In this master thesis, the objective is to find the influence of phase fraction, grain size and local composition in ferritic-martensitic steels on the corrosion properties of the steel. The main objective is to perform only heat treatments on the given samples, while keeping the base material composition the same. The mentioned microstructural features can be altered by performing different heat treatments; the resulting corrosion properties are expected to change. To independently investigate the influence of the microstructural features, both fully martensitic as ferritic-martensitic microstructures need to be produced.

The martensitic samples will be used to investigate both the influence of prior austenite grain size on the corrosion properties and to find the dependence between pitting behaviour and prior austenite grain size. The ferritic-martensitic samples will be used to investigate the influence of the phase fractions on the corrosion rate as well as the influence of local composition on the corrosion rate of the martensite regions in the alloy.

Chapter 2

Experimental procedure

This chapter describes the experiments that were done to obtain results about both metallurgy and corrosion properties. First, the used samples will be described, along with the experiments to perform the right heat treatments. The corrosion experiments will also be described, along with information on how to interpret their results.

2.1 Material

For the experiment, commercial dual-phase (DP600) steel was used, as produced by TATA Steel [28]. This steel alloy consists of both ferrite and martensite in the form of martensite bands around the ferrite grain boundaries.

2.1.1 Composition

In order to know the exact properties of the steel, the composition of the samples was examined. The DP600 sheet from TATA Steel [28] was first cut in 10x5x2 mm pieces. Since the sheet was zinc-coated, the samples were sanded (up to grid 180) and rinsed with ethanol to expose a clean steel surface. An analysis was performed, by doing X-Ray Fluorescence

Element	Fe	C	Mn	Cr	Si	Al	Ni
Weight percentage	balance	0.092	1.543	0.512	0.351	0.057	0.036

Table 2.1: Weight percentage of alloying elements in steel samples

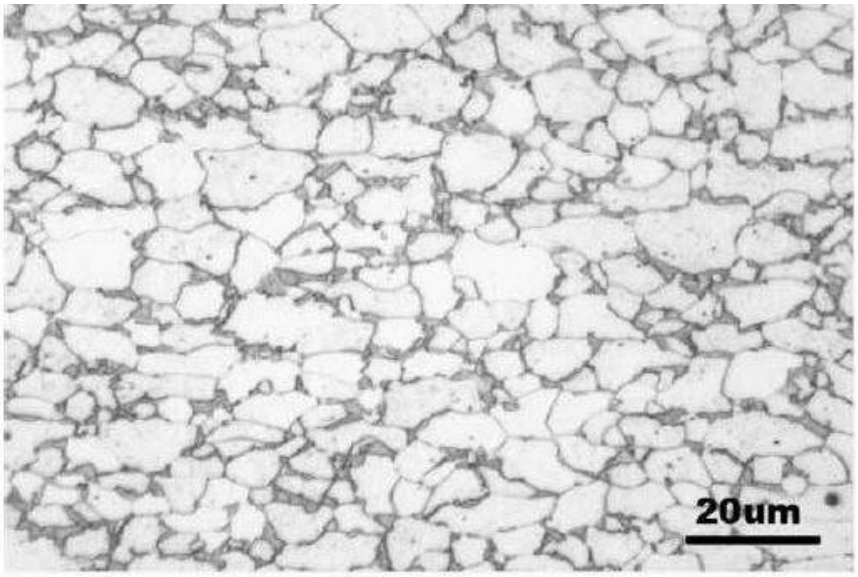

Figure 2.1: Microstructure of a DP600 steel, showing the white ferrite regions and grey martensite, surrounding the ferrite grains [5].

spectroscopy, using a Panalytical Axios Max WD-XRF spectrometer. Data analysis was performed using SuperQ5.0i/Omnian software. During XRF measurements, the composition of a sample can be examined by measuring the wavelength (thus energy level) of re-emitted X-rays. The results of the XRF analysis are shown in Table 2.1, showing the weight percentage of each alloying element in the steel. Note that carbon content could not be measured due to equipment limitations, so it was assumed this was similar to values of previous research using the same alloy [29]. With Equation (1.1) and the composition as in Table 2.1, the martensite start temperature was found to be $M_s = 444°C$.

2.1.2 Original microstructure

Figure 2.1 shows a typical commercial dual-phase (DP) ferrite-martensite microstructure that was etched with Nital etchant. Ferrite is displayed in light grey, while martensite is shown as dark regions in the microstructure. The martensite in the DP steels is known for its high strength, due to the slightly deformed crystal structure (BCT). The softer ferrite, around which the martensite was found, will accommodate a sliding mechanism for the martensite, due to its lower hardness. This combination of strength and de-

formability makes the dual-phase alloys very well suited for the automotive industry [30, 31, 32, 33].

The DP600-alloy was chosen since the composition is well suited for the desired heat treatments. A normalization step was performed before the annealing heat treatment would take place. By holding the material at a high temperature for a certain time, the introduced strengthening mechanisms such as precipitates (ternary phase particles) or dislocations were removed. The duration of this normalizing step also determined the amount of grain growth that would occur.

2.1.3 Intercritical annealing

Since the initiation of new phase and growth is not instantaneous, the holding time in the intercritical region will determine the size of the phases and the amount that has been developed. This means that, when the sample has been normalized in the austenite region (above the A3-temperature), it takes time for ferrite to nucleate in the austenite. The lower the temperature, the higher the driving force for nucleation. When the driving force is low, nucleation will mostly be heterogeneous. Heterogeneous nucleation will not occur globally through the lattice, but will occur at microstructural imperfections such as grain boundaries or precipitates. When the driving force is higher, nucleation will also occur within the bulk of the austenite grains.

Intercritical annealing was performed to obtain ferrite and austenite in the microstructure. After quenching, the austenite is transformed into martensite, giving the desired ferritic-martensitic microstructure.

2.1.4 Phase fraction measurements

The modelled phase fractions, from the phase diagram, are, due to limitations in the equipment, expected to differ from the obtained phase fraction in the samples. Therefore, measurements needed to be done to determine the actual phase fractions in the samples. When the microstructure was visible in the optical microscope, the different phases could be distinguished.

To obtain results about the phase fractions, first, a grid was projected on top of each image, having 15x11 intersections between vertical and horizontal lines. According to the ASTM standard [34], at each of these intersections

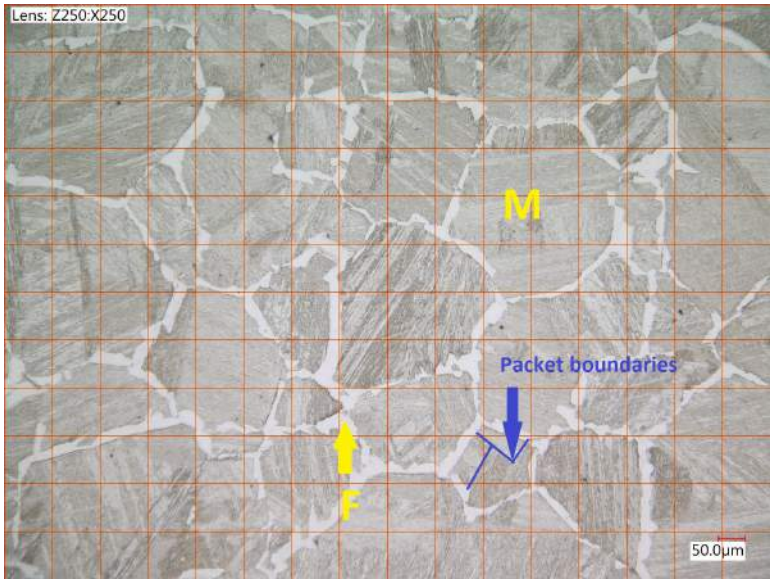

Figure 2.2: Microstructure with projected grid lines; dark regions are martensite (M), light regions are ferrite (F); blue lines are packet boundaries with the martensite regions.

the underlying phase needed to be examined visually whether it was ferrite or martensite. By averaging the counted amounts over all the projected intersections, the average phase fractions were obtained. Figure 2.2 shows a sample microstructure with corresponding grid overlay.

Attention must be paid to the fact that the microstructure was not homogeneous over the entire surface due to the higher cooling rate on the clamped sides. To correct for this, the phase fraction was (for each sample) measured for two positions in the center of the sample and two positions on the edges.

2.1.5 Grains in different phase morphologies

Figure 2.2 shows, besides grid-lines, different phases in a ferritic-martensitic dual-phase sample. The dark regions in the figure are the martensite regions, while the bright regions are composed of ferrite. As mentioned before in Section 1.1.3, martensite is not simply built up out of grains, but laths, blocks and packets were observed as substructures. It can be clearly seen that the colour of the martensite regions is not homogeneous: the blue lines,

for example, display the boundaries between different packets. Due to these inhomogeneities, the prior austenite grain size is taken as a measure for martensite grain size, since those can be distinguished from the optical images easily as being the entire dark regions.

It can be seen that the martensite regions are surrounded by narrow ferrite bands, which have been initiated on the prior austenite grain boundaries. The ferrite grains appear to be homogeneous, since the colour is similar over the entire surface. Unfortunately, it was hard to distinguish between the various ferrite grains, since no grain boundaries were visible in between. Therefore, the grain size of ferrite was not taken into account.

2.1.6 Grain size measurements

Both dual-phase samples and fully martensitic samples will be produced for the electrochemical experiments. The dual-phase samples will be used to investigate the influence of phase fractions and local composition. The fully martensitic samples will be used to determine the influence of grain size on corrosion properties.

When determining the grain size of the martensite in the fully martensitic samples, it was hard to measure the actual laths of the martensite, since they usually are small in the order of $0.5\mu m$ [13, 15]. The difference between the various prior austenite grains was easier to observe, and the prior austenite grains were expected, due to the high energy level of the boundaries in between, to have the biggest influence on corrosion properties. The size of the martensite regions in the ferritic-martensitic samples was considered as well and is defined as the square root of the area in between the nucleated ferrite bands.

To determine the size of the grains, the boundaries of it needed to be transferred to a transparent sheet. This transfer was done manually, since the known software was not able to distinguish between the various grains, where the human eye is. Image analysing software, called ImageJ [35], was used to measure the area of the various grains from a scanned image of the transparent sheets. The output of the software was a table with area in square micrometers and the amount of measured grains.

Using Microsoft Excel 2010, a distribution was made of the found grains to determine whether grains of certain sizes were preferred. The grains size

distribution is generally shown in a plot in which on the x-axis, the prior austenite grain size or size of the martensite regions (for the dual-phase samples) is shown, while on the y-axis the fraction of grains or regions, having that size, are shown. A distinction can be made between the number fraction of grains and the area fraction. The number fraction will show how many grains have a size in the mentioned window. One could however imagine that the contribution of small grains to the corrosion properties is smaller than that of big ones. Therefore, the area fraction was used to display the fraction of sample area that was covered by grains that have a size in the mentioned window. From the area fraction, an average grain size and standard deviation were calculated.

2.2 Methods

This section explains the used techniques to fabricate the samples, including heat treatments and sample preparation, and the electrochemical measurement techniques.

2.2.1 Thermo-Calc

Thermo-Calc is a software package that is able to perform thermodynamic calculations and construct phase diagrams. Given a certain alloy, its composition, system size and the environment (temperature and pressure), Thermo-Calc is able to calculate the equilibrium phases. To construct a phase diagram, several thermodynamic equilibrium calculations were done at different temperatures. The resulting phase diagram differs from the previously mentioned iron-carbon phase diagram, since more than two elements were present in the sample.

When the composition is fixed, as was the case here, the amount of phase can be calculated as a function of temperature. This means that when for example a ferrite fraction of 0.25 was needed, Thermo-Calc was able to find the corresponding annealing temperature in the intercritical regime.

Since Thermo-Calc has a database with thermodynamic parameters, the local compositions in the different phases could be calculated as well. The solubility of alloying elements was known, so a plot will be made which showed the fraction of each of the elements in austenite as a function of the ferrite fraction.

Note that Thermo-Calc was not able to calculate data for martensite since that is not an equilibrium phase. It is however assumed that quenching is rapid enough that the composition and phase fraction is similar for the martensite as it was for the stable austenite (at temperatures in the intercritical regime).

2.2.2 Dilatometry

To perform the heat treatments on the samples, a dilatometer was used. The term dilatometer is coming from the word dilatation, similar to expansion. A quenching- and deformation dilatometer, type Bähr Dil 805 A/D, was used to heat-treat the samples [36, 37]. The working principle of a dilatometer is based on two basic functions: first, accurate heating and cooling can be performed by means of an induction coil around the sample in a vacuum chamber and the possibility to flush the chamber of the dilatometer with helium to provide cooling. Using the coil, very high heating rates can be achieved since the samples are small in size and thus have a very low heat capacity. The helium, depending on the flow, can be used to cool or quench the sample. A combination of heating and helium flow will also allow the user to cool the sample slowly.

The other feature of the dilatometer is the ability to measure the change-in-length of the samples. Upon heating, the sample will expand as a function of temperature, due to an increased lattice parameter in the crystal structure. The strain can be measured and is, divided by the temperature, equal to the thermal expansion coefficient. When a phase transformation occurs, for example the transition from BCC to FCC iron, the thermal expansion coefficient of the sample will change, since it is different for every crystal structure. The A1- and A3-temperatures can be therefore found by verifying at which temperature the slope in the dilatation versus temperature curve becomes straight again. The volume of a unit cell is different for FCC and BCC, therefore, a change-in-length (or actually volume) can be seen in the dilatometer as well after a phase transformation.

To measure the temperature of the sample in the feedback loop of the heating section, a thermocouple was attached to the sample. This thermocouple, made out of two thin platinum wires, was welded on the steel surface. The disturbances in the steel microstructure as a result of this welding process were assumed to be small, since the platinum wires were small compared to the sample size.

The samples were, as mentioned, 10x5x2 mm in size; the size was needed to be this small to be able to maintain a quenching rate that was high enough for martensite to form. The samples were clamped in between two quartz clamps, which were attached to the expansive section of the dilatometer. Attention must be paid that when the normalizing temperature was above 1100°C, as was the case for several samples, the standard quartz clamps of the dilatometer could not be used any more due to creep. The high temperature is then too close to the melting point of quartz. Alumina was used instead, but this gave some problems: the thermal expansion coefficient for alumina is $5.4*10^{-6}K^{-1}$, compared to $0.7-1.4*10^{-6}K^{-1}$ for quartz [38]. This means, that the dilatation was no longer negligible compared to that of steel: $10 * 10^{-6}K^{-1}$. The dilatation data was therefore not fully reliable any more, since any found dilatation could be caused by either the sample or the clamps (or a combination of both). Also, the thermal conductivity was higher for alumina, so more heat was withdrawn from the sample into the clamps, resulting in more undercooling at the sides of the sample.

2.2.3 Sample preparation

After the dilatometric heat treatment, a copper wire was soldered to the top of the sample. This was done to maintain electrical contact between the electrochemical measuring equipment and the sample. The samples were embedded in Struers ClaroCit resin and cured for 1 hour. The resin was also covering the copper wire to prevent solution from entering and forming a galvanic couple between the copper wire and steel samples. The embedding was done for easy handling during polishing of the samples and to provide extra protection and support during further preparation. Next, the samples were wet ground using grit 80, 180, 320, 800, 1200 and 2000 SiC paper, of which the latter has a particle size of 9μm. During the grinding, the samples were often rinsed with ethanol to prevent corrosion of the surface and to flush away dirt that could be embedded in the resin. After grinding, the samples were polished using diamond particle-based slurry, first with 3μm and later 1μm particles, until no more scratches or dirt was visible in the microscope. Finally, the samples were ultrasonically cleaned for 5 minutes in ethanol, dried and stored in a dessicator. A dessicator is a glass bell filled with crystals that absorb moisture and prevent the samples from corroding. The storing in between polishing and electrochemical experiments was never more than 10 minutes to make sure that the surface was as clean as possible, since over time (even in a dessicator) a natural oxide layer will form.

To prevent the occurrence of crevice corrosion in the seam between the sample and the resin, this seem was covered with a thin layer of sealing lacquer, Electolube Bloc Lube Red. One other benefit of this layer was that the corroded area could be measured accurately, since this was the entire exposed area inside the lacquered surface.

2.2.4 Optical microscopy

To observe the results of the performed heat treatments, the microstructure needed to be investigated. Besides looking at the data from the dilatometer, optical images were taken of the microstructure. However, the polished samples did not show any features under the microscope besides a smooth surface. Therefore, the polished samples needed to be etched to reveal the grains of the different phases. With an etchant, certain features (phases, grain boundaries) will be corroded to be able to distinguish between them. An etchant generally is an acid; for these experiments Nital 2% was used, which is a solution of 2wt% of nitric acid dissolved in alcohol. The working principle of the etchant is based on preferential attack of the etchant to high-carbon regions. This means that the martensite and the grain boundaries were etched more than the ferrite, causing the ferrite to be coloured relatively light, compared to the martensite.

To etch the samples, they were first rinsed with ethanol again. After this cleaning step, the samples were gently swiped with a cotton pad which was soaked in Nital 2%. This was done for a duration of 17 seconds. This duration was chosen as an optimum after trial and error on a dummy sample. Finally, the samples were rinsed with ethanol again to remove any etchant residue and then again ultrasonically cleaned in ethanol for 5 minutes.

The optical images were taken using a Keyence VHX-5000 digital optical microscope, using a VH-Z20R/W/T objective, capable of magnifying between 20 and 200 times and a VH-Z250R/W/T objective, capable of magnifying between 250 and 2500 times. The benefit of using this microscope over others is the fact that this one is operated fully digital. Therefore, focussing and scanning over the surface could be done accurately.

When the optical inspection of the samples was finished, the Nital layer needed to be removed again. Therefore, a few minutes polishing with $1\mu m$ diamond slurry was sufficient. This polishing made the sample smooth again

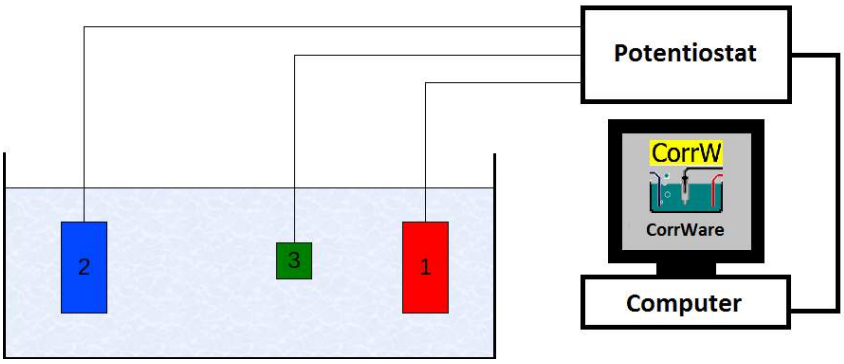

Figure 2.3: Schematic drawing of the 3-electrode electrochemical cell with: (1) sample (working electrode), (2) counter electrode and (3) reference electrode as well as a potentiostat and a computer

and prevented the Nital from influencing the results of the electrochemical experiments.

2.2.5 Electrochemical polarization measurements

For the electrochemical measurements, a standard 3-electrode electrochemical cell was used in which a potential can be applied over the sample with respect to a reference through which the resulting current was measured. Figure 2.3 shows a sketch of the 3-electrode cell setup; the three electrodes can be seen, immersed in the electrolyte and coupled to a potentiostat. A potentiostat is an apparatus that is coupled to a PC and is able to apply and measure potentials and currents. A potentiostat has a feedback-loop built-in, providing accurate control over the applied potential. The number 1 electrode is the working electrode, which is the sample during these experiments. The number 2 electrode is an inert counter electrode, not taking part in the reaction, and is chosen to be made of carbon for these experiments. The counter electrode is used to close the electric circuit between the working electrode and the potentiostat and conducts the electric current. Electrode 3 is the reference electrode, which has a fixed potential independent of the solution parameters, and can therefore be used to measure the potential difference between itself and the sample. This reference was chosen to be a Ag/AgCl electrode, which consists of a glass tube filled with saturated potassium chloride (KCl) solution that is connected with the

solution through a porous cap [39, 40]. In the KCl-solution, a silver wire is submerged which has been coated with silver chloride and is connected to the rest of the setup. The potential of this electrode will not change due to the balance between the silver- and the potassium-chloride, provided that the electrolyte will remain saturated with KCl. The potential of the electrode was fixed with respect to the Standard Hydrogen potential at +0.224V.

During the open-circuit potential (OCP) measurements, the potential difference was measured in between the working electrode and the reference electrode. The open circuit potential was defined as the potential over the working and reference electrode when the circuit was not closed. This means that once the open-circuit potential has been established, no current can be measured. Since the potential level of the reference electrode was not changing, the potential development of the sample can be measured as a function of time. A change in OCP will normally be caused by the development of a passive layer on the metal surface, which will develop during the submersion of the sample in the electrolyte.

After the OCP measurement, the sample was polarized. During this experiment, a potential has been applied over the working and reference electrode. A current flowed as a result, since the working electrode was corroding. This current was measured using the potentiostat and was displayed as a function of applied potential. The current changed as a result of the corrosion process that took place on the sample surface. OCP measurements are mostly performed before the polarization to stabilize the situation of the steel in the solution. This was done since the natural oxide layer first has to dissolve when the sample was just submerged.

Electrochemical cell

For these experiments, a specially designed 3-electrode cell was made using PMMA (*poly(methyl methacrylate)*) as building material. As a change in the distance from sample to both the reference and the counter electrode could influence the diffusion rate, it was important to keep this distance the same during each of the experiments. To solve this problem, the cell was equipped with a hole in the bottom, surrounded by a ring. In this ring, the mounted specimen was tightened, over the hole. Through two holes in the top, the counter electrode and the reference electrode were lowered, making sure they were at the same position every time. This corrosion cell setup is shown in Figure 2.4.

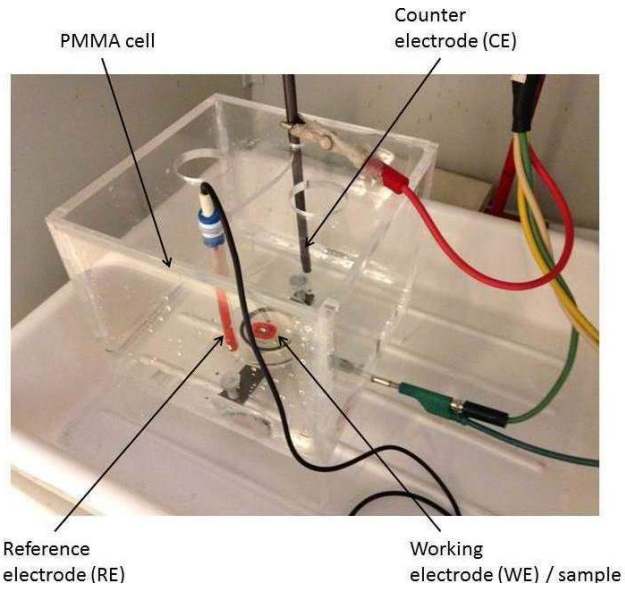

Figure 2.4: PMMA corrosion cell with sample mounted at the bottom (with the red lacquer applied) as working electrode and both the counter and reference electrodes immersed from the top.

The entire setup was placed in a Faraday cage to remove any electromagnetic noise that was present in the surroundings and could influence the measurements. The three mentioned electrodes were connected to a Schlumberger Solartron SI1286 potentiostat, which was coupled to a Windows PC using a National Instruments GPIB-120A Bus Expander/Isolator. The used software, to measure and vary the potential, was CorrWare for Windows, version 3.3c. Finally, the values for corrosion rate were calculated using the Rp-fit algorithm in CorrView for Windows, version 3.3c.

Electrolyte

Previous research has been done using 3.5wt% NaCl solution (0.6M) in water as an electrolyte [18, 19, 20, 25]. This electrolyte was chosen, since it shows similarities to sea water. The NaCl content in sea water is around 3.5wt% as well, depending on water depth and position, and can be seen as a worst-case scenario due to the high chlorine concentration.

Polarization parameters

The corrosion experiments on the entire sample were performed in the following order: first determining the open circuit potential, secondly polarization and finally the inspection of the surface using the optical microscope.

The open circuit potential was measured for 5 minutes. Generally, longer submersion times are used, but the active nature of the steel in the 3.5wt% NaCl solution gave rise to corrosion when the common duration of 30 minutes was used. The polarization experiment, after the OCP, was started at a potential of -250mV versus the obtained open circuit potential. In this region, the cathodic behaviour of the sample can be investigated. Then, following a rate of 0.5mV per second, the potential was increased to higher values until the potential reaches +250mV versus OCP. During this polarization, the current started negative (cathodic current) but increased to positive values (anodic current) as the applied potential became higher than the corrosion potential.

The results of these experiments were displayed in a log current density versus potential diagram. The current density of the corrosion reaction (i) was displayed as a function of the applied potential (E). An example of such a curve is shown in Figure 2.5. The figure shows the cathodic process in the bottom part of the curve, please note that here the absolute current density ($|i|$) is displayed, since the sign of the potential is reversed in the cathodic regime as compared to the anodic regime.

Corrosion potential and current density

The corrosion potential and current density could be obtained by drawing tangents to the straight parts of both the anodic and cathodic curves, as displayed in Figure 2.5. The x-coordinate of the point at which both tangents intersect is defined as the corrosion current density and the y-coordinate as the corrosion potential.

Another method to obtain the corrosion potential and current density is the so-called Rp-fit method, which was used during the course of this research. The resistance of the total setup was assumed to be constant around corrosion potential and corrosion current density. At the point where the current changed sign, the potential was measured. By fitting the slope of the E vs. i (potential vs current density) curve, the resistance was measured.

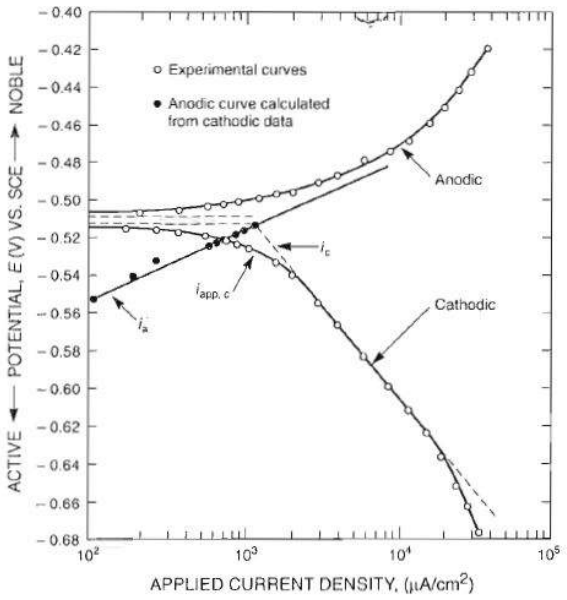

Figure 2.5: Polarization curve, potential versus current density diagram, showing the anodic and cathodic branches [4].

Finally, by dividing the potential by the resistance, the corrosion current density was calculated. An advantage of this method is the fact that it can be performed by the computer and is less sensitive to human interpretation of the results.

2.2.6 Optical corrosion inspection

To investigate which corrosion mechanism was leading for the martensitic samples with varying prior austenite grain size, the same PMMA cell was used, although no electrodes or potentiostat were coupled now. The martensitic samples were mounted in the holder and then submerged in 100mL of the same 3.5wt% NaCl solution as was used before. After 10 minutes, the samples were taken out of the solution, cleaned with ethanol and observed under the optical microscope. The objective of this was to see where the corrosion started to initiate. After taking photos with the microscope, the samples were submerged for another 20 minutes and observed again. Finally, the samples were submerged for a third time, this time for 30 minutes, bringing the total submersion time to 60 minutes.

The optical images were taken using the same Keyence digital optical microscope as before with its high contrast to see initiation clearly. The images will show the amount of corrosion products on the surface and whether corrosion happens locally or across the entire specimens surface.

2.2.7 Micro-capillary electrochemical cell

For measuring the influence of local composition, the corrosion properties of martensite alone had to be examined, since the presence of ferrite will influence the results. Therefore, a very local technique was used to make sure other grains did not influence the measurement. For this reason, a micro-capillary cell was used. This cell is in general based on the principle of the conventional 3-electrode electrochemical cell as explained above.

Key difference between the conventional 3-electrode electrochemical cell and the micro-capillary cell is the size of the measured area. Where the exposed area of the conventional cell had a diameter of several centimeters, the maximum size for the micro-capillary cell was $100\mu m$ during these experiments. The preparation of the tips for this type of measurement was complicated, as was previously explained in [29, 41, 42]. The capillary was first produced by pulling heated (hollow) glass tubes until they broke, leaving a tapered end. The initial internal diameter of these tips was 0.8mm. The pulled tip, still closed at the end at which the two halves broke apart, then needed to be grounded and polished, to open up the tip. The ratio between inner and outer diameter remained fixed during the pulling, which is a property of the glass that was used for the tubes. As a results of this, the inner diameter of the opening could be calculated from the outer diameter by multiplying it with this ratio. Inner diameters could vary between 20 and $1000\mu m$, depending on the time spent sanding. After sanding, the tip was flushed with ethanol and coated with silicone to ensure proper sealing on the surface since the glass surfaces never were fully flat. Since the silicone caused the glass not to touch the steel surface, it also prevented crevice corrosion from occurring between the glass and the sample.

When the silicone has dried, the tip was placed in a holder containing the 3.5wt% NaCl-solution, a platinum counter electrode and the Ag/AgCl reference electrode, of which the latter was connected through a tube filled with electrolyte as well. The entire holder was attached to the carousel of a microscope, where normally the objectives are placed. The advantage of this support was both the rigidity of the microscope frame as the possibility

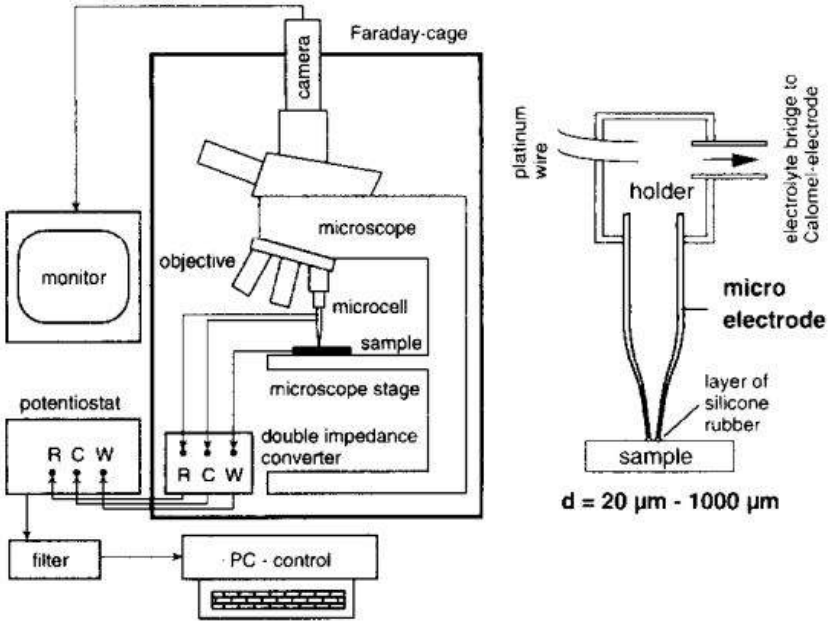

Figure 2.6: Schematic sketch of the setup for the micro-capillary cell [6]

to optically determine the exact spot of the tip on the surface, simply by swivelling to one of the objectives of the microscope. The tip was then pressed onto the steel surface until the silicone started to flex in order to ensure proper sealing and to facilitate electrical contact between the sample and the electrolyte. This entire setup was placed in a copper Faraday cage, since the small currents (down to the pico-ampère range) could be influenced by external disturbances, such as radiation from cell phones. The current density and potential were measured using a Swiss Microcell Systems SMS V 0301 and Electrochemistry software, version 2004, by the Swiss Society for Corrosion Protection. A sketch of the measurement setup is shown in Figure 2.6. The right part of the image shows the holder in which the tip is mounted as well as the platinum counter electrode. The left part of the image shows the microscope framework with the holder mounted in the carousel and the three wires providing the electrical conduction towards the potentiostat.

Parameters

The small diameter of the tip was expected to give rise to problems when a similar polarization trajectory would be chosen as was the case for the conventional 3-electrode electrochemical cell. The cathodic polarization would initiate a layer of reaction products on the surface. Unfortunately, when the sample area as small as was the case with the micro-capillary cell, this layer could block the glass capillary, preventing electrical contact from occurring. A similar effect was observed when the anodic current became too high. Therefore, after an OCP measurement of 5 minutes, the polarization was started at -75mV with respect to the obtained open circuit potential. Then, at a rate of 0.5mV per second, the potential was increased to +125mV versus OCP. The corrosion potential and the current density were derived using the Rp-fit method as was explained before in Section 2.2.5.

Attention should be paid when the data of the micro-capillary cell were to be compared with data for the conventional polarization experiments, since the currents would differ. This is caused by the resistance of the micro-capillary cell being much bigger as compared to the conventional cell due to a smaller volume of electrolyte.

Micro-capillary placement

Since the effects of local composition needed to be measured very accurately, the placement of the tip must also be very accurate. To determine the spots in which the tip should be placed, the surfaces were etched using Nital 2% for 15 seconds. This made the microstructure visible under the optical microscope and grains were selected to place the capillary in, preferably large martensite regions to reduce the risk of placing the tip in ferrite by accident. These grains were marked using micro-indents at the prior austenite grain boundaries. Per sample, 3 martensite regions were selected. Figure 2.7 shows an optical image of the indents, shown as the dark diamond shapes.

Since the Nital etchant would influence the corrosion measurements, the surface was polished subsequently with $1\mu m$ diamond slurry. This polishing step removed the etchant residues, the top layer of the etched areas and provided a clean surface. After polishing, a 24 hours waiting time in the dessicator was introduced to allow the natural oxide layer to develop fully [43]. When this waiting time would not be considered and the electrochemical measurements were to be performed directly, the time between polishing

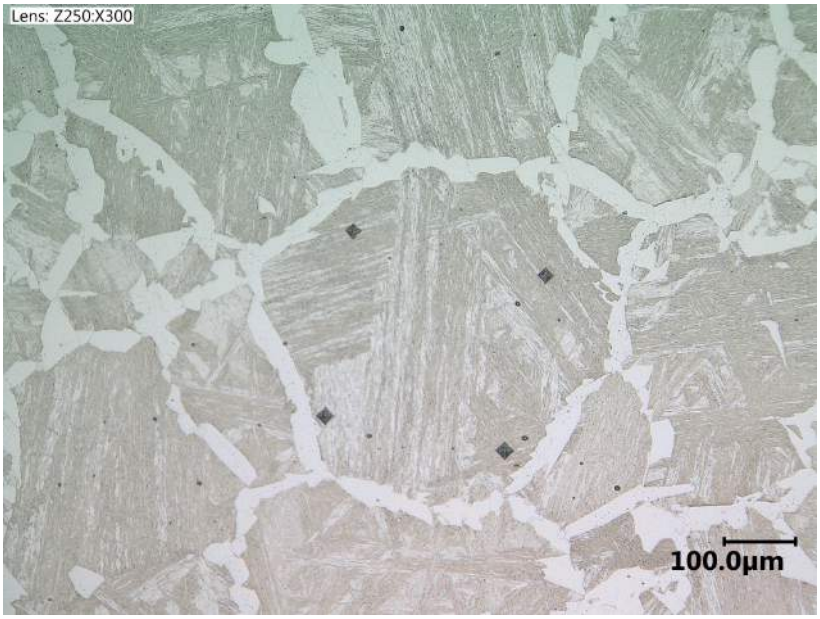

Figure 2.7: Optical image of the (dark, diamond-shaped) indents in the martensite regions of sample DP3

and experiments would be different for each of the three spots per sample, since the three experiments could not be performed simultaneously. The oxide layer after 24 hours was assumed to be in equilibrium with the environment, meaning it has stopped growing and (the part that was not in contact with the electrolyte) was thus not changing during the experiment.

Chapter 3

Results and discussion

In this chapter, the results of the various experiments will be shown and will be discussed as well. Conclusions about occurring mechanisms or possible irregularities will also be mentioned.

3.1 Microstructure making

This section explains the obtained microstructures; first, the phase diagram for this alloy is constructed with Thermo-Calc, then, the parameters for the dilatometric experiment are shown. After this, the results of the dilatometer curves are shown, followed by the optical images of the microstructures and the data for the phase fractions and grain size distribution.

3.1.1 Phase diagram with Thermo-Calc

Figure 3.1 shows a phase diagram, as was made with Thermo-Calc, which displays the equilibrium phases in the actual alloy, given the composition as in Table 2.1. On the x-axis, the carbon content is shown, together with a red line at 0.092wt%, which is the carbon content in the tested alloy; the y-axis displays the temperature in Kelvin. In the figure, besides the expected lines for the A1- and A3-temperature, another line is present which displays the equilibrium temperature for cementite, an iron-carbon intermetallic (Fe_3C). Below this purple line, the cementite will be stable, together with austenite and ferrite. The extra alloying elements, with respect to the iron-carbon situation in Figure 1.2, apparently stabilized the cementite at higher temperatures.

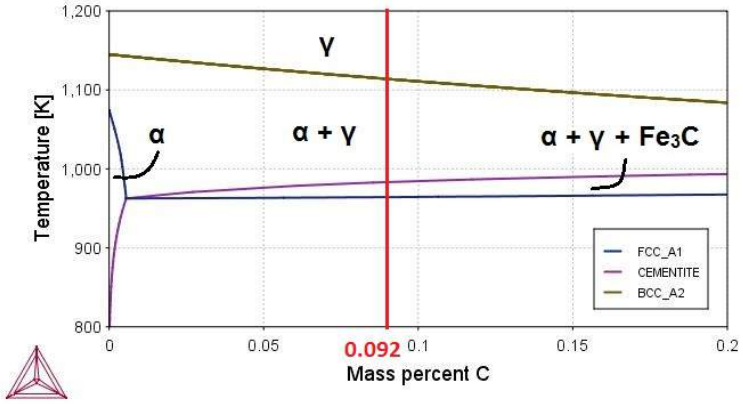

Figure 3.1: Phase diagram of the tested alloy, obtained using Thermo-Calc

The A1- and A3-temperatures for the tested alloy can be read in Figure 3.1. It was found that the A1-temperature is 965K (692°C). The A3-temperature was found to be 1115K (842°C). The phase transformations in the dilatometer are therefore expected to occur between 692 and 842°C. However, the undercooling and overheating to initiate both the ferrite and austenite respectively are expected to change this temperature window. The annealing temperature for the dual-phase samples needs to be taken in this intercritical region (taking the undercooling into account) to be sufficient for ferrite nucleation on the austenite grain boundaries.

Figure 3.2 is made using Thermo-Calc as well and shows, for the alloys composition as in Table 2.1, the amount of phase as a function of the temperature. It can be seen that for temperatures below 965K (692°C) only BCC ferrite is present along with cementite (pink lines), displayed by the the very high and very low concentration line respectively; until the A1-temperature, the ferrite fraction is not changing with temperature. When the temperature is increased towards the intercritical region ($\alpha+\gamma$), austenite will start to nucleate. This is shown by the green and blue line, with austenite fraction starting at 0% for 965K and ending at 100% for 1115K. Above 1115K, the A3-temperature, only austenite will be present and the cementite particles have been dissolved. The intercritical heat treatments will be performed at 700°C and quenched afterwards to form martensite out of austenite. It can be seen in Figure 3.2 that a low amount of austenite and carbides will be present and the microstructure would be mostly ferritic.

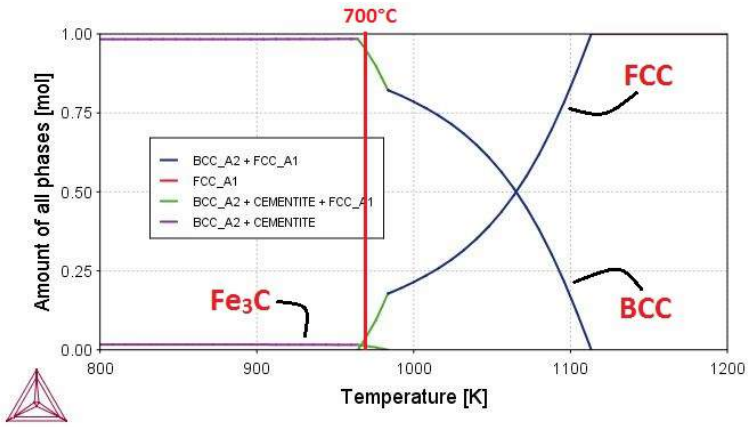

Figure 3.2: Amount of phase as function of temperature

3.1.2 Input parameters for dilatometry

Martensitic microstructures For the martensitic samples, normalizing in the austenitic regime will already result in a martensitic microstructure after quenching. To vary the grain size of the martensitic samples, the samples were normalized at 900, 1000 and 1100°C. These three temperatures were assumed to result, as can be seen in Figure 3.1, in an austenitic microstructure. The heating rate towards the normalizing temperature was 10 Kelvin per second, starting from room temperature. The holding time at the normalizing temperature was chosen to be 10 minutes to allow significant grain growth to occur. After normalizing, the samples were fully quenched by purging the chamber with helium until the temperature would reach room temperature again. The heat treatments for the martensitic samples are displayed in Figure 3.3 in which the temperature is displayed versus the time. The three different heat treatments can be seen, displaying clearly the heating trajectories, the different normalizing temperatures as well as the quenching at the end of the normalizing step.

Ferritic-martensitic microstructures The dual-phase samples were normalized as well, prior to the intercritical heat treatment. Big prior austenite grains were desired for the purpose of micro-electrochemistry to avoid misplacement of the micro-capillary tips. The normalization temperature was therefore chosen to be 1200°C, with a heating rate of 10 Kelvin per second; the duration was 30 minutes. After the normalization, one sample was quenched towards room temperature, using helium again. The remain-

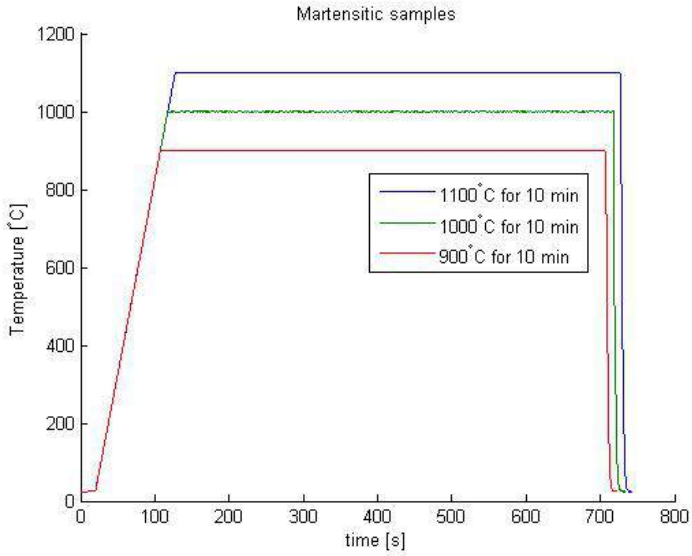

Figure 3.3: Sketch of the temperature versus time curve, as was used as input for the dilatometer to perform the martensitic heat treatments

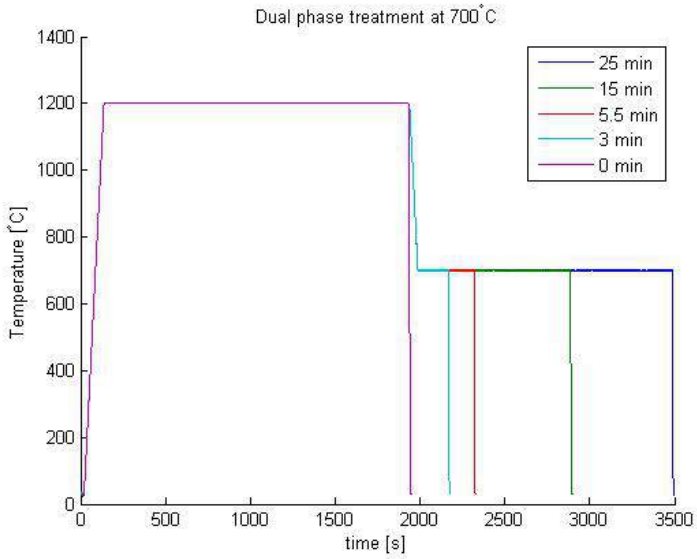

Figure 3.4: Sketch of the temperature versus time curve, as was used as input for the dilatometer to perform the dual-phase heat treatments

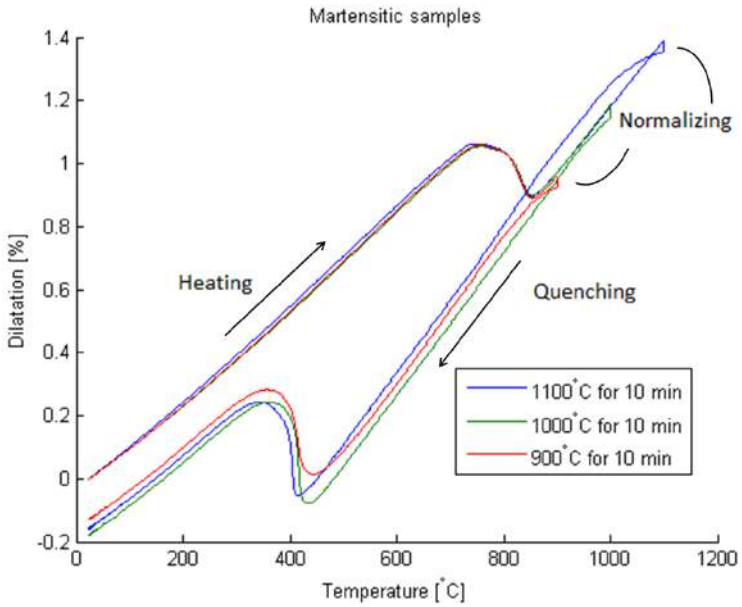

Figure 3.5: Dilatation versus temperature for martensitic samples

der of the samples, four in total, were cooled to 700°C, in the intercritical region; the chamber remained under vacuum, no helium flow was needed. Different annealing times were handled, 3 minutes, 5.5 minutes, 15 minutes and 25 minutes. After this intercritical annealing, ferrite should have been nucleated in the austenite matrix, preferentially on the austenite grain boundaries. The samples were then quenched towards room temperature using the helium flow again. Figure 3.4 shows the heat treatments in a temperature versus time diagram.

3.1.3 Dilatometry curves

Martensitic samples

First, the dilatometry curves for the martensitic samples are shown in Figure 3.5; the dilatation is shown as a function of temperature. The curves start at room temperature, with the dilatation being zero. Upon heating, the dilatation increased linearly with increasing temperature, due to the thermal expansion. At 730°C, the phase transition from BCC ferrite to FCC austenite is shown. The dilatation here was no longer linear, since the volume for an FCC unit cell is lower than that of a BCC cell [10]. At a temperature of 840°C, the lines became linear again, marking the A3-temperature and

a fully FCC microstructure was obtained. These A1- and A3-temperatures were similar for every sample, since the heat treatments were similar so far. The measured A1-temperature (730°C) was shown to be different from the calculated equilibrium temperature of 695°C. This difference is caused, as expected, by a certain amount of overheating that was required to initiate austenite in the ferrite. The A3-temperature was found to be similar for both measured as calculated cases. This is a straightforward result, since for the total dissolution of ferrite in austenite no overheating is required. At the normalizing temperatures (1100, 1000 and 900°C), a small change in dilatation could be seen. This is caused by the growth of the austenite grains and the reduction of grain boundaries, resulting in a higher density of the samples, since the voids between atoms on the grain boundaries were initially occupying volume, but had not mass.

When the sample was quenched, the dilatation decreased again, as is shown in the lower part of the curves in Figure 3.5. A linear drop can be observed until temperatures of around 450°C. This temperature was well below the A1-temperature of the sample. However, this A1-temperature was calculated in the equilibrium situation and quenching is highly transient. The measured transformation temperature coincided with the calculated martensite start temperature of $M_s = 444°C$ from Section 2.1.1. It can be observed as well that the phase transformation, the non-linear part of the curve, would occur first (during quenching) for the sample that was normalized at the lowest temperature. This is caused by the difference in austenite grain size between samples [44, 45], since the sample that was normalized at 900°C had less grain growth, thus more grain boundaries per unit volume. It has been seen that grain boundaries are favourable nucleation sites during cooling, so the sample with the highest grain boundary density would start to transform first.

Finally, it can be seen that the phase transformation towards martensite was finished first for the 900°C normalized sample. The final dilatations, when the samples were back at room temperature, were shown to be below 0. This means that the samples have shrunken during the heat-treatment process. This shrinkage is caused by the fact that another microstructure was present as well as the process of grain growth and reduction of the grain boundary density. It can be seen that the final microstructure was different than before (BCT crystal structure), since the slope of this final part of the curve was slightly lower as compared to the first part of the curve, in which martensite and ferrite were present.

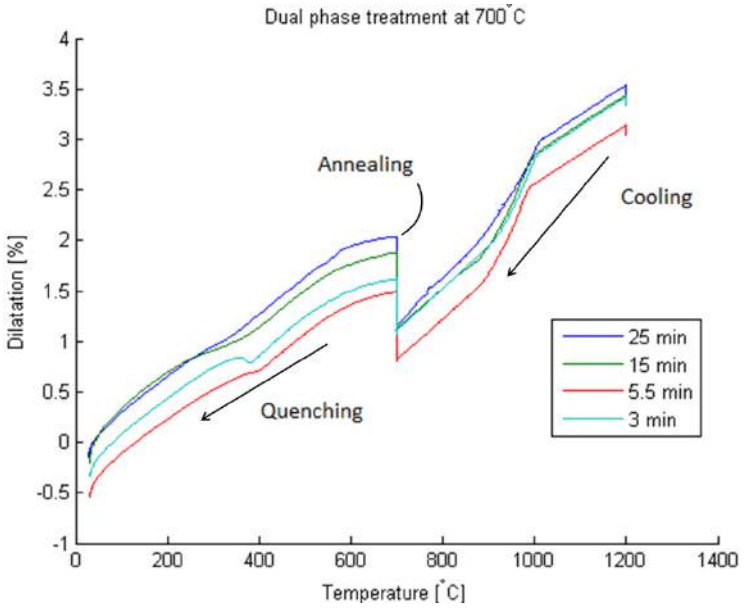

Figure 3.6: Dilatation versus temperature for dual-phase samples

Ferritic-martensitic samples

Figure 3.6 shows the temperature versus dilatation curve for the dual-phase, ferritic-martensitic, samples. The heating part of the curves was removed, since it was similar for all samples. After the normalization, the sample was cooled. The first change in slopes, around 950°C, was caused by the alumina clamps. After that, no change in slope was seen until the annealing temperature at 700°C. At that temperature, the ferrite has been nucleated, after which the samples were quenched. It must be mentioned that the alumina clamps prevented the dilatation curves to be useful; the red curve, for example, is expected to be in between the curves for 3 and 15 minutes annealing, since the ferrite fraction was expected to be in between as well.

Figure 3.7 shows the development of the dilatation with respect to time. It can be seen that during the first 1800 seconds, the sample expanded up to a certain level. There, the slope decreased and the dilatation became constant. After the cooling to the intercritical region, between 1800 and 2000 seconds, the dilatation was shown to increase again. This is caused by growth of ferrite, having the larger lattice parameter, within the austenite. It could be seen that for the shortly annealed samples, with 3 and 5.5 minutes

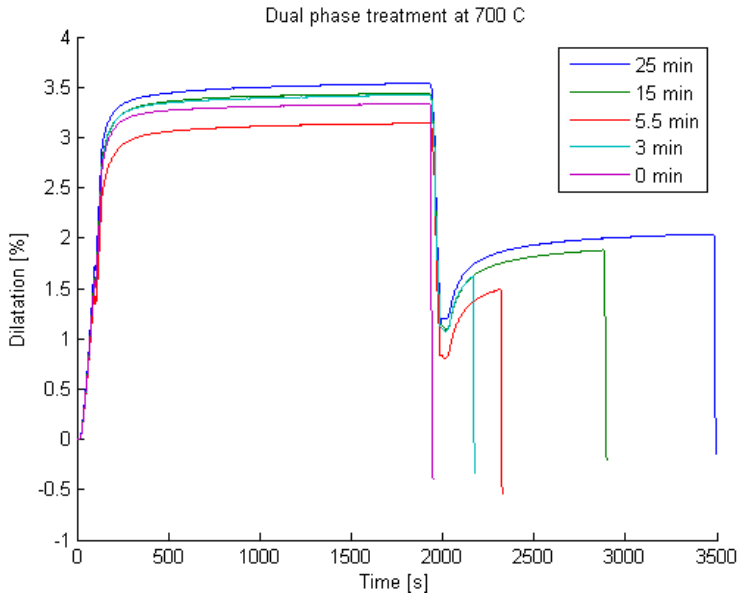

Figure 3.7: Dilatation versus time for dual-phase samples

holding time in the intercritical region, the dilatation would not reach an equilibrium length. This means that the ferrite has not fully grown yet in the austenite at the point where they were quenched. With other words, the shortly annealed samples had less ferrite than was predicted by the (equilibrium) calculations with Thermo-Calc. Since the dilatation reached an equilibrium value for the 25 minutes-annealed sample, this sample is expected to have the calculated equilibrium ferrite fraction. Besides that, the nucleation of ferrite demands a certain amount of undercooling [11]; the found ferrite fraction during the transient cooling will be therefore lower compared to the equilibrium case that is displayed in Figure 3.2.

3.1.4 Microstructures

Figures 3.8, 3.9 and 3.10 show the microstructures of the obtained martensitic samples. The magnification of Figure 3.8 is 250x, while that of Figures 3.9 and 3.10 is 500x. In the figures, different shades can be observed in the microstructures, which are the various prior austenite grains and were made visible by polarising the light of the microscope. This polarization caused the reflection of different planes in the martensite to be in different shades. Within the prior austenite grains, needle-like textures were observed. These

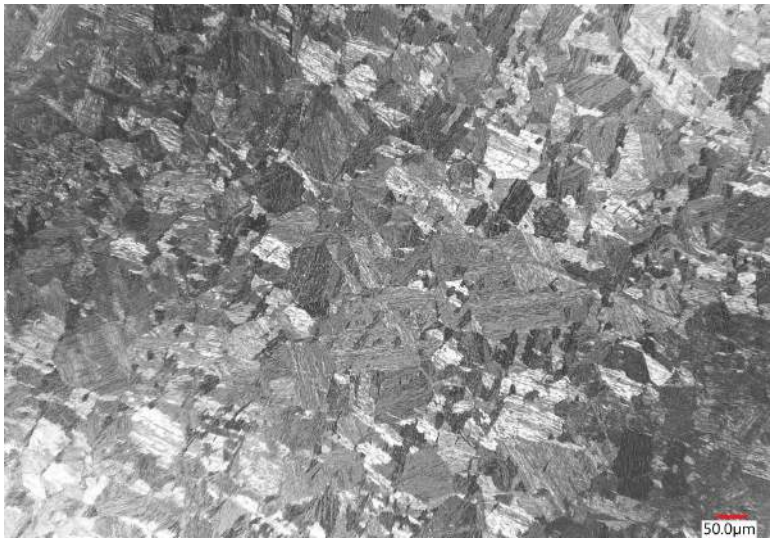

Figure 3.8: Optical image, magnification 250x, of martensitic sample M2, normalized at 1100°C; scale bar: $50\mu m$

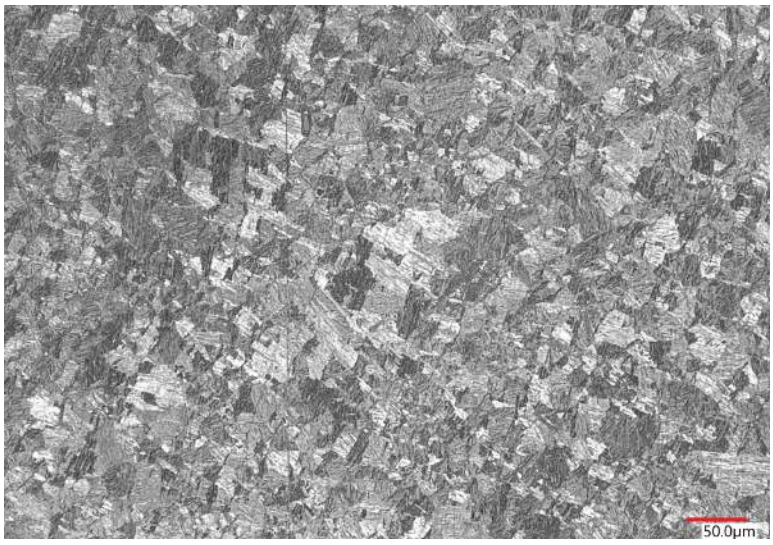

Figure 3.9: Optical image, magnification 500x, of martensitic sample M3, normalized at 1000°C; scale bar: $50\mu m$

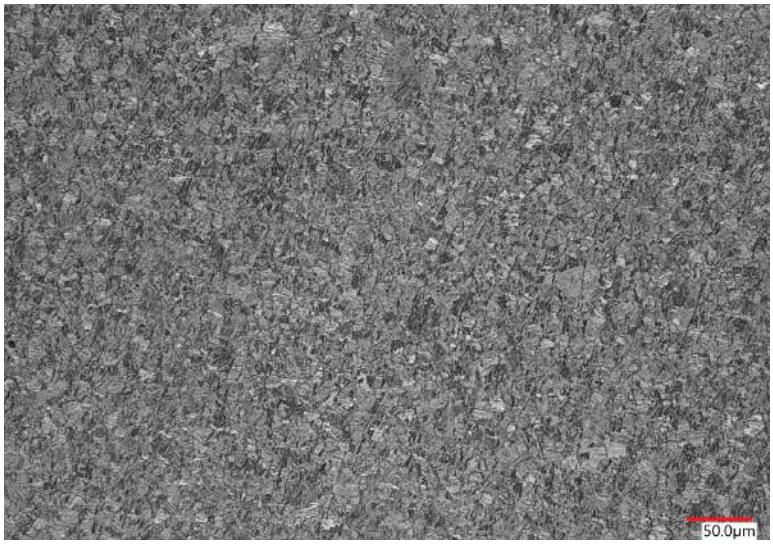

Figure 3.10: Optical image, magnification 500x, of martensitic sample M4, normalized at 900°C; scale bar: $50\mu m$

are the laths, and are clustered in the packets which share laths in the same direction. Table 3.1 displays the heat treatment and sample codes for the martensitic samples.

In Figures 3.11 until 3.14, the dual-phase microstructures are shown. The martensite is displayed in the dark regions, while the ferrite is displayed light grey. It can be clearly seen in Figure 3.14 that the ferrite was only present at the prior austenite grain boundaries, since the ferrite encircles the martensite in narrow bands. With increasing annealing times, the amount of (dark) martensite was reduced.

When the microstructures of the DP1 and DP2 samples were observed, in Figures 3.11 and 3.12, it can be seen that ferrite would nucleate within

Sample	Heat treatment
M2	1100°C 10 min, *quench*
M3	1000°C 10 min, *quench*
M4	900°C 10 min, *quench*

Table 3.1: Heat treatment and sample codes for martensitic samples

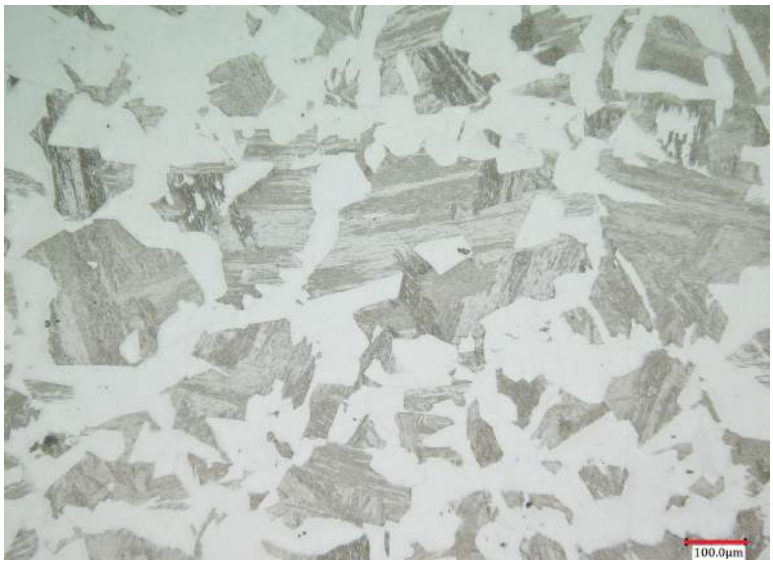

Figure 3.11: Optical image, magnification 250x, of dual-phase sample DP1, annealed at 700°C for 25 minutes; scale bar: $100\mu m$

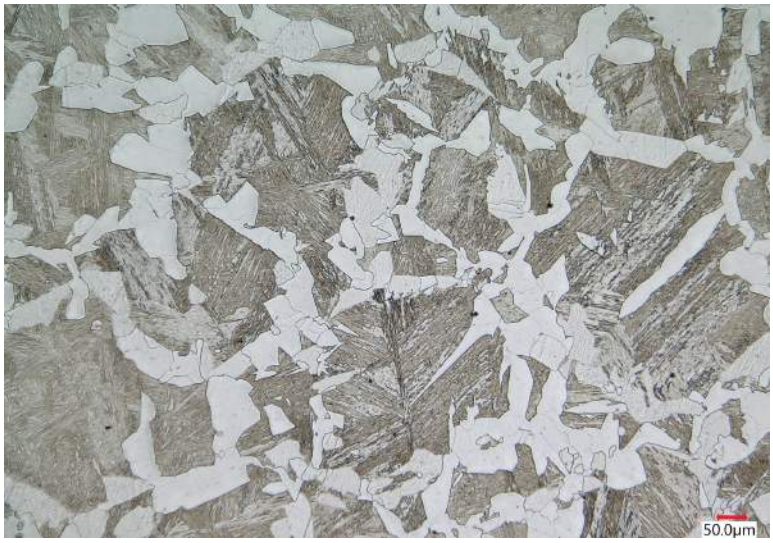

Figure 3.12: Optical image, magnification 250x, of dual-phase sample DP2, annealed at 700°C for 15 minutes; scale bar: $50\mu m$

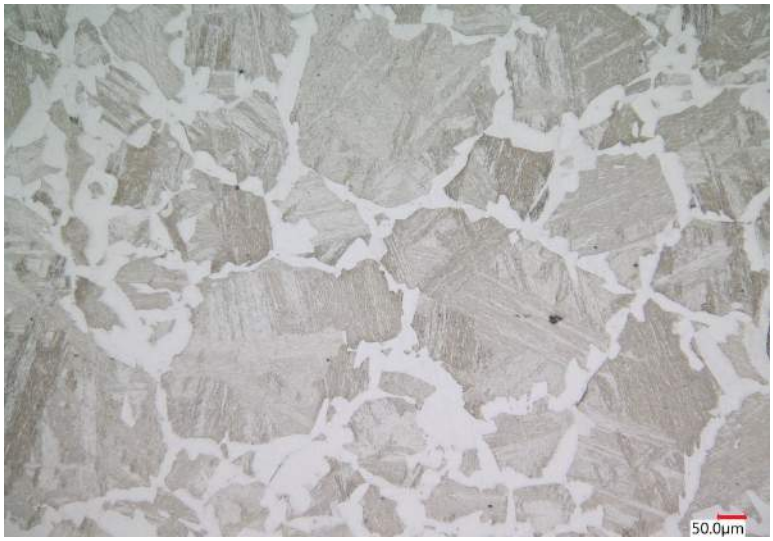

Figure 3.13: Optical image, magnification 250x, of dual-phase sample DP3, annealed at 700°C for 5.5 minutes; scale bar: $50\mu m$

Figure 3.14: Optical image, magnification 250x, of dual-phase sample DP4, annealed at 700°C for 3 minutes; scale bar: $50\mu m$

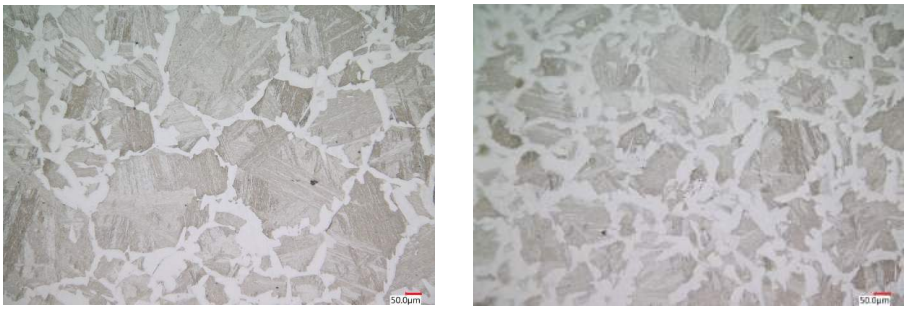

Figure 3.15: Optical micrographs for sample DP3, with left showing the center of the sample and right the edge of the sample; scale bar: $50\mu m$

the austenite grain and not only on the prior austenite grain boundaries, as a result of the long annealing times. Therefore, when the micro-capillary electrochemical cell would be used to measure localized corrosion properties, the placement of the tip would become increasingly difficult with increasing ferrite fraction, since the martensite regions became relatively small.

Finally, it was observed that a difference in microstructure existed between the center of the samples, where the thermocouple was attached and the sides, where the clamps were attached to the sides of the sample. Figure 3.15 shows the difference between the microstructure in the center of the sample (on the left) and the edge of the sample (on the right), with the one at the edge having a higher amount of ferrite and smaller martensite regions. The heat transport towards the alumina clamps did lower the temperature on the side of the sample, reduced the amount of grain growth and increased the amount of undercooling in favour of the ferrite nucleation. To accommodate for this difference, both the grain size distribution and the phase fractions were measured for regions across the entire sample instead of only a local region.

3.1.5 Phase fractions

In Table 3.2, the phase fractions for the dual-phase samples are shown. It can be seen that with increasing annealing time, the ferrite fraction was increasing, as was also observed in the dilatation vs. time curves in Figure 3.7.

It can be seen that the standard deviation of the phase fraction increases

Sample	Heat treatment	Fraction martensite (α')	Fraction ferrite (α)
DP1	700°C 25 min	0.478 ± 0.0803	0.522 ± 0.0803
DP2	700°C 15 min	0.555 ± 0.0859	0.445 ± 0.0859
DP3	700°C 5.5 min	0.664 ± 0.0431	0.336 ± 0.0431
DP4	700°C 3 min	0.854 ± 0.0158	0.0146 ± 0.0158

Table 3.2: Phase fraction of ferrite and martensite in ferritic-martensitic dual-phase samples

with ferrite fraction. In the microstructures, Figure 3.11 until 3.14, it was seen that the ferrite initially (for short annealing times and low fractions) nucleated at the austenite grain boundaries in an ordered way. When the samples were annealed longer, it was seen that ferrite nucleated in the bulk of the austenite grains as well, giving a larger spread across the sample.

3.1.6 Element distribution in martensite

Now that the obtained phase fractions are known, the local composition of the martensite could be calculated. It was seen before, in Section 1.1, that the solubility of alloying elements is higher in FCC austenite than in BCC ferrite. This means that when the ferrite fraction was increased, the amount of enrichment of alloying elements in the austenite increased as well. Thermo-Calc was used to simulate the intercritical heat treatments and to find the concentration of alloying elements in the martensite. The results are shown in Figure 3.16, in which the composition of alloying elements is shown as a function of ferrite fraction. The black lines represent the actual concentration of elements in the martensite, while the red lines display the global content in the sample.

In Figure 3.16, it is shown that the carbon, manganese, chromium and nickel concentration would increase in the martensite with respect to the global content. Silicon and aluminium, both being metals used for the killing (de-oxidising) of steel [46], partitioned in the ferrite since the concentration in martensite was found to decrease. The biggest relative increase in concentration was found for carbon: factor 2 when 50% of ferrite was introduced. However, the concentrations of alloying elements in this alloy are relatively low, since the steel is preferably low-alloyed to obtain a dual-phase microstructure. The local differences in concentrations are therefore expected to have a small effect, mostly caused by the change in manganese fraction, which had the highest weight percentage.

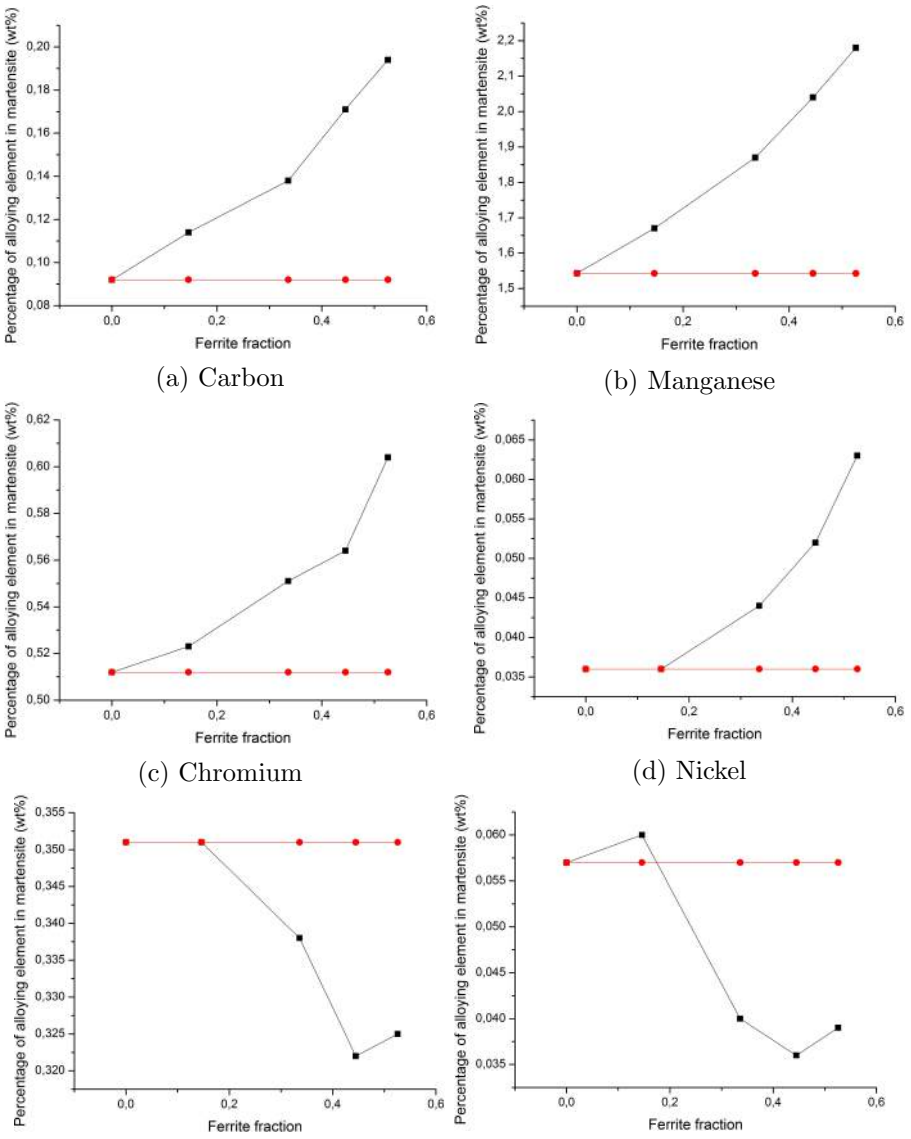

(a) Carbon

(b) Manganese

(c) Chromium

(d) Nickel

(e) Silicon

(f) Aluminium

Figure 3.16: Weight percentage of alloying elements in the martensite as a function of ferrite fraction

Sample	Heat treatment	Average grain size
M2	1100°C 10 min, *quench*	$41.4\mu m \pm 26.24$
M3	1000°C 10 min, *quench*	$22.3\mu m \pm 10.31$
M4	900°C 10 min, *quench*	$8.6\mu m \pm 4.13$

Table 3.3: Average prior austenite grain size for martensitic samples

3.1.7 Grain size distribution

Martensitic samples

Figure 3.17 shows the prior austenite grain size distribution as was obtained for the martensitic samples M2 to M4. On the x-axis, a range of grain sizes is displayed, increasing $5\mu m$ every step. The y-axis displays the number fraction in black and the area fraction in blue. When the area fraction of prior austenite grains is observed ,in Figure 3.17, it can be seen that the area fraction of the sample normalized at 1100°C was shifted the most to the large grains. The width of the prior austenite grain size distribution seemed to increase with increasing normalizing temperature (and thus prior austenite grain size), which was caused by a less uniform microstructure, in which not all the grains were to have similar sizes. This increasing prior austenite grain size with increasing normalization temperature was also observed in the optical images. The number fraction displays that the highest amount of prior austenite grains, for all martensitic samples, lies below the average grain size, that was obtained using the area fraction.

Table 3.3 summarises the heat treatments for the martensitic samples and shows the average prior austenite grain sizes, with standard deviation. It can be seen that the average prior austenite grain size increased with increasing normalizing temperature. However, the average grain size had a large standard deviation coupled, increasing with increasing average grain size. This increase is not the result of an error in the measurements but caused by the wider spread in grain sizes.

Ferritic-martensitic samples

Figures 3.18 until 3.21 show the distributions of area and number fractions of the martensite regions in the dual-phase samples. The x-axis displays the grain size, the black and blue bars the number and area fraction respectively. Ferrite was found to initiate at the prior austenite grain boundaries and grew from here towards the interior of the austenite. The observed area

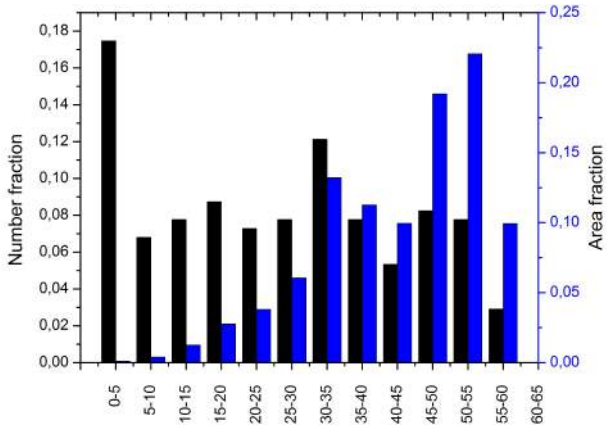

(a) M2: 1100°C for 10 minutes

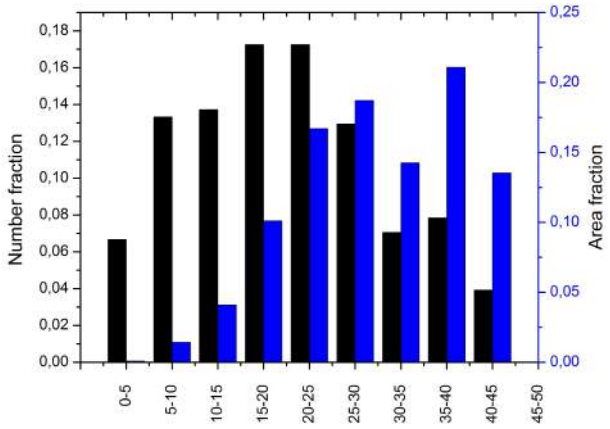

(b) M3: 1000°C for 10 minutes

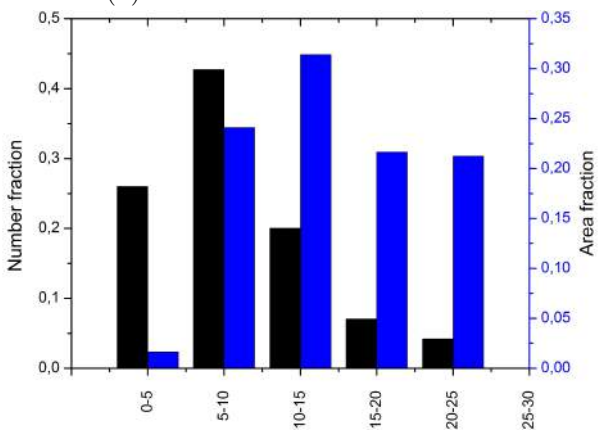

(c) M4: 900°C for 10 minutes

Figure 3.17: Prior austenite grain size distributions for martensitic samples; black bars represent number fraction, blue bars represent area fraction, on the x-axis, prior austenite grain size is displayed

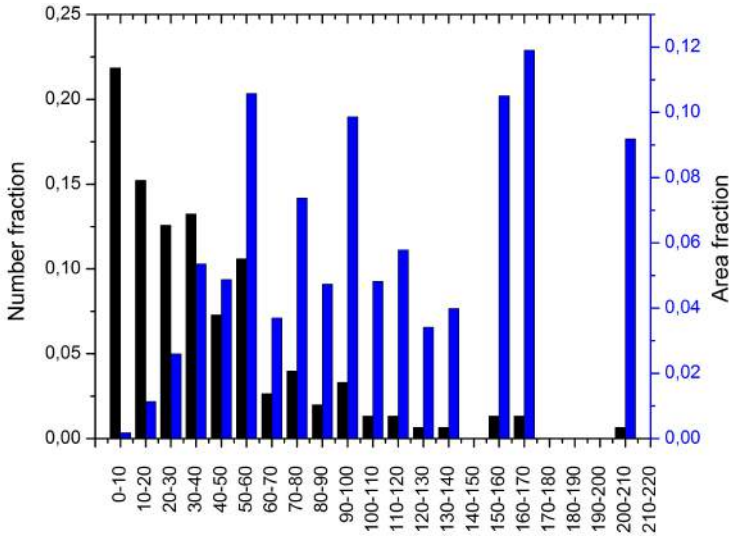

Figure 3.18: Distribution of the number and area fractions of the martensite regions in ferritic-martensitic sample DP1: 700°C for 25 minutes

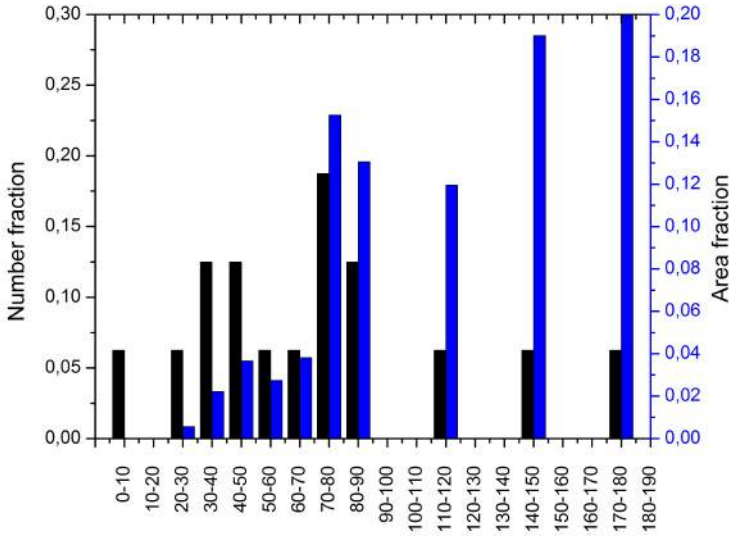

Figure 3.19: Distribution of the number and area fractions of the martensite regions in ferritic-martensitic sample DP2: 700°C for 15 minutes

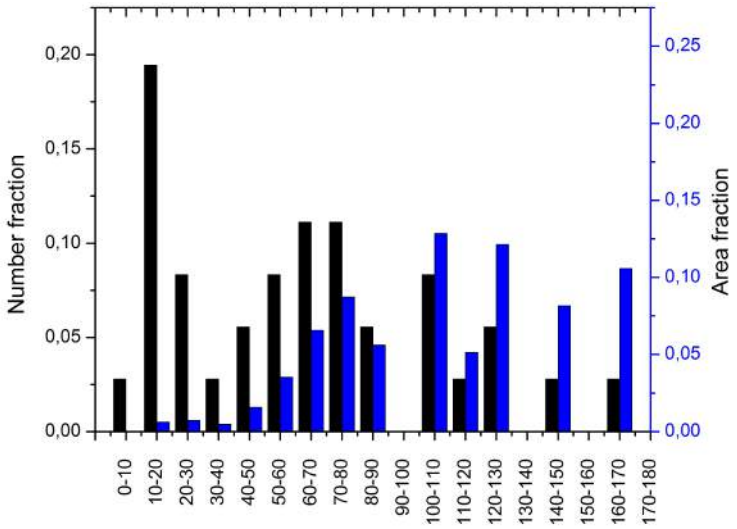

Figure 3.20: Distribution of the number and area fractions of the martensite regions in ferritic-martensitic sample DP3: 700°C for 5.5 minutes

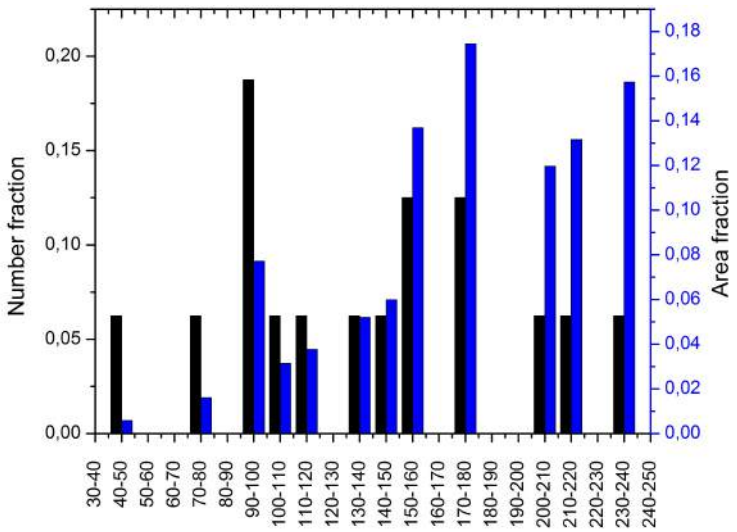

Figure 3.21: Distribution of the number and area fractions of the martensite regions in ferritic-martensitic sample DP4: 700°C for 3 minutes

Sample	Heat treatment	Median size of the martensite region
DP1	700°C 25 min	$30 - 40$
DP2	700°C 15 min	$60 - 70$
DP3	700°C 5.5 min	$60 - 70$
DP4	700°C 3 min	$130 - 140$

Table 3.4: Median size of the martensite regions in the ferritic-martensitic samples

fraction of the martensite regions in the dual-phase samples was therefore shifting to lower sizes when more ferrite grew.

The distributions in Figures 3.18 to 3.21 show that for the shortly annealed samples, the largest area fraction was shifted more towards the larger martensite regions. The number fraction of grains also shifted to larger regions when the annealing times became shorter. It can be seen in the figures that the width of both the number fractions and area fractions distributions remained large for all samples. This means that a wide variety of martensite region sizes was present in all samples.

Table 3.4 summarises the dual-phase heat treatments of samples DP1, DP2, DP3 and DP4. When the average sizes of the martensite regions were calculated, the resulting values were similar to each other. From the optical images, however, it was clear that the martensite in the different samples, did not have similar sizes. Therefore, the median value of the number fraction distributions was taken: the martensite region size, corresponding to the center value of the distribution, is mentioned in the table for each sample. This indeed shows the shift towards larger martensite regions for shorter annealing times.

3.2 Influence of prior austenite grain size on corrosion properties

The martensitic samples were tested for their global corrosion properties by polarizing them in the mentioned 3-electrode electrochemical cell. First, the OCP was measured and after that, the sample was polarized. Figure 3.22 shows the resulting curves from these polarizations. On the y-axis, the applied potential is displayed, with respect to the standard hydrogen reference potential, while the x-axis shows the resulting current density that was measured during polarization. Note that, due to the large window of currents, the scale on the x-axis is a log scale.

The polarization was started at a potential of -250mV versus the OCP. It can be seen that, for low potentials, the curve is very steep; this means that the current varied very little with the applied potential. From that observation, it must be concluded that some factor must limit the current there, since otherwise the current is expected to increase with more negative potentials. At the cathode, dissolved oxygen was reduced to form oxygen ions. This process consumed electrons and the oxygen ions would recombine with water to form hydroxyl ions, as was seen in Reaction (1.9). The limiting process at low potentials can be explained by a limited supply of oxygen towards the cathode, which will retard the cathodic reaction. The cell volume was large, compared to the sample area, meaning that enough oxygen was present in the electrolyte. The supply of oxygen towards the cathode (the diffusion process) must therefore be the limiting factor, caused by the small sample size and area at which the reduction reaction took place.

When the polarization was continued, it can be seen in Figure 3.22 that the current density started to decrease rapidly, roughly above an applied potential of $-0.50V$. Although generally not displayed in polarization curves (due to the log scale), the current changed sign here, since the reaction mechanism changed from consuming electrons to supplying electrons to the potentiostat. For the metal, this sign change meant that the reaction process changed from hosting the oxygen reduction reaction (by supplying electrons) towards the oxidation of iron, by which electrons and iron ions were produced. When the potential was increased further, the dissolution of iron atoms became the leading reaction mechanism. It can be seen that at these potentials, the current was rapidly increasing with a small increase in potential. The limiting factor of diffusion was not present here, since the reactant

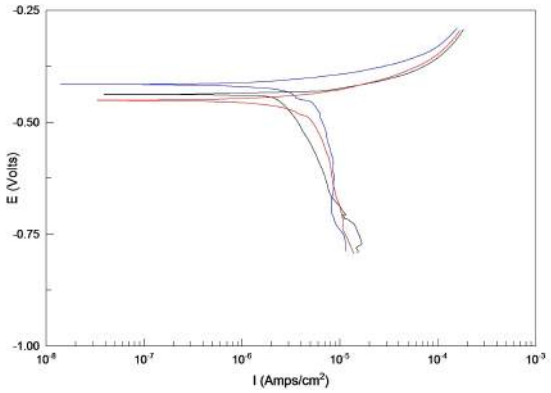

(a) sample M2, average PAGS: 41.4μm

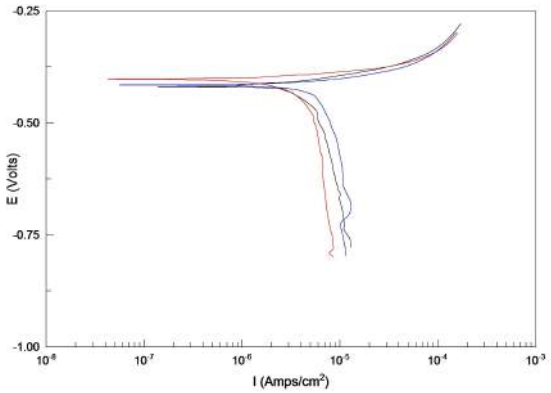

(b) sample M3, average PAGS: 22.3μm

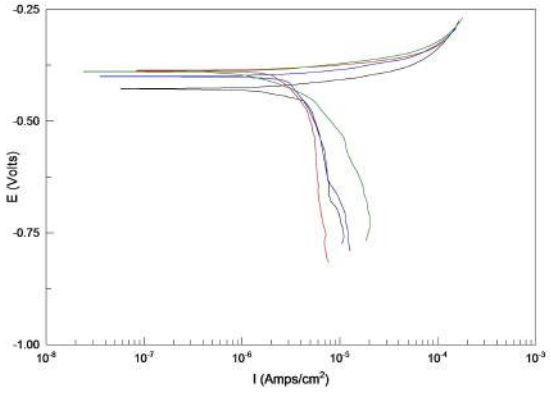

(c) sample M4, average PAGS: 8.6μm

Figure 3.22: Polarization curves for martensitic samples, the average prior austenite grain size (PAGS) is mentioned under each figure

(iron) was present in solid form. At some point, around a current density of approximately $10^{-4} Acm^{-2}$, the slope of the curve started to increase. At this point, the dissolution of iron started to become limited and varied less with applied potential. The iron was still present in solid form, so the supply of iron to the reaction is not likely to become limiting. The diffusion of ions, away from the anode, is not likely to become limiting either, since the saturation limit of iron ions in water is high. The build-up of a layer of iron-hydroxide $Fe(OH)_2$ reaction products on the surface, as was predicted by Reaction (1.11), can be a cause of the limited dissolution. This layer forms a barrier between the iron and the electrolyte and prevents the iron from getting into contact with the electrolyte. The limited reaction kinetics will result in a smaller increase of current density with increasing potential.

It must be noted that the passive (vertical) part of the polarization curve is not clearly visible in Figure 3.22. Generally, polarization curves will have a vertical part in which the material behaves passive[4] and the current density remains constant with increasing potential. From this, it must be concluded that this alloy is active over a wide potential range and shows little passivity. Other research on comparable alloys [19] also showed the active behaviour, without the passive trajectory.

The corrosion potential has been estimated from the polarization curves and is displayed in Figure 3.23 for all three martensitic samples. The potential is displayed versus prior austenite grain size; the values for corrosion potential are shown as well in Table 3.5. Despite the standard deviation of the prior austenite grain size to be large, the corrosion potential was found to decrease with increasing prior austenite grain size, which was caused by a decrease in grain boundary density. The grain boundaries were earlier found to be more active than the surrounding bulk of the grains [21, 22]. A decrease in prior austenite grain boundary density is therefore expected to decrease the total activity of the sample.

Sample - PAGS	**Corrosion potential** (mV)	**Current density** $(\mu A/cm^2)$
$M2 - 41.4\mu m$	-239 ± 13.6	40.9 ± 1.82
$M3 - 22.3\mu m$	-215 ± 6.0	48.0 ± 7.96
$M4 - 8.6\mu m$	-205 ± 13.6	56.2 ± 11.91

Table 3.5: Corrosion potential and current density of martensitic samples

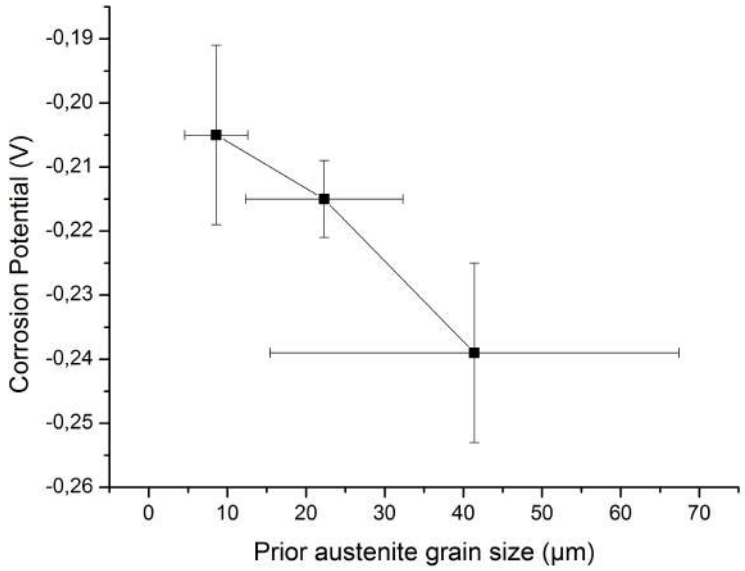

Figure 3.23: Corrosion potential for the martensitic samples, with error bars for the width of the grain size distribution (x-direction) and measured potential values (y-direction)

Logically, an increase in the grain boundary density was expected to increase the activity of the sample resulting in a less noble situation (with lower, more negative potential). However, a less noble site on the surface not necessarily needs to have a lower corrosion potential. To verify the reactive behaviour of grain boundaries, the corrosion current density could give insight in the corrosion rate of the martensitic samples. The corrosion current density is shown in Figure 3.24 versus the prior austenite grain size and its values in are mentioned in Table 3.5 as well. It can be seen that for decreasing prior austenite grain size, the current density would increase. This means that for smaller prior austenite grains, thus a higher grain boundary density, more dissolution of iron would occur and the corrosion rate will be higher. This is a logical result of the increased activity of the sample with a high prior austenite grain boundary density, since activity represents the ability to corrode in a certain environment. The increase in error for the current density is caused by the increased complexity of the sample, since more prior austenite grain boundaries were present of the surface.

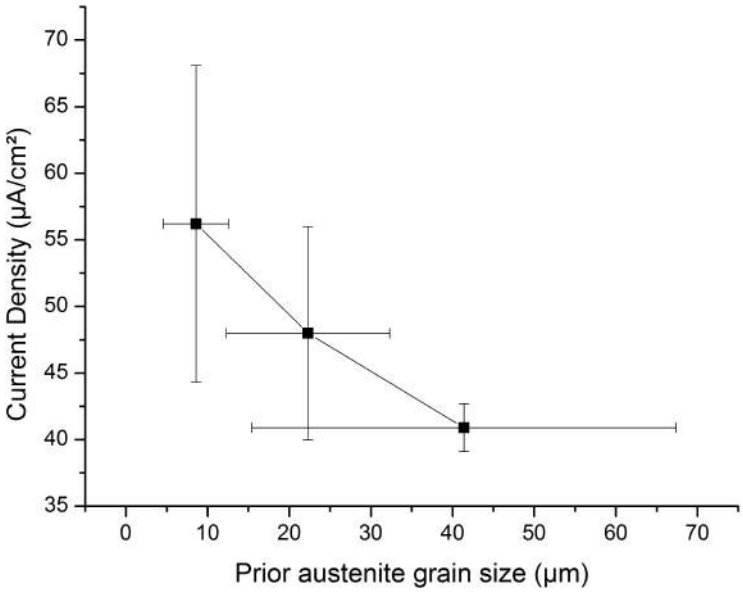

Figure 3.24: Corrosion current density for the martensitic samples

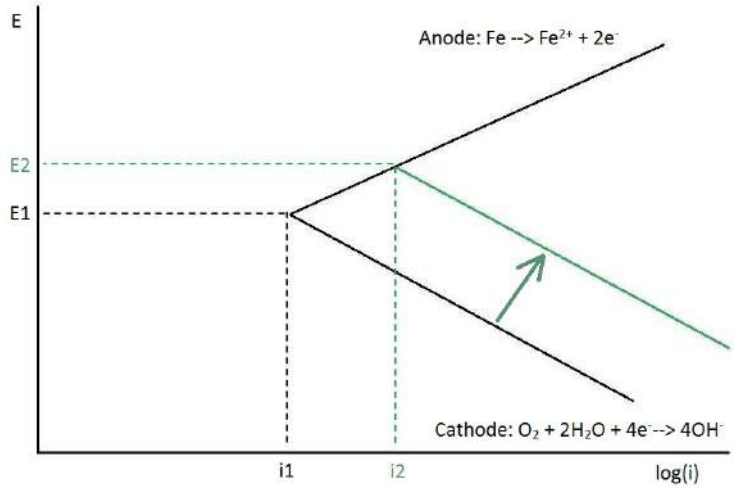

Figure 3.25: Sketch of theoretical potential versus log(current density) curve, showing increase in corrosion potential when cathode current density increases (from black to green)

Considering the increased corrosion rate for the samples with smaller prior austenite grains, it can indeed be concluded that a higher grain boundary density will increase the activity of the samples. In Section 1.2, the cathodic reaction was seen to be limiting for this process due to the limited amount of oxygen that reacted at the cathode surface. An increase in current density, which has been found to occur for smaller prior austenite grains, therefore will be caused by a change in the cathodic reaction. In Figure 3.25, a sketch of a polarization curve is shown; the green curve shows a shifted cathodic curve with respect to the black initial curve, caused by an increased cathode current density. The anodic curve is still similar to the initial one. However, it is observed that the exchange potential and corrosion current density (at the intersection of both curves) will both be higher. This result was indeed found during the experiments, as can be seen in Figures 3.23 and 3.24.

Summarizing this experiment, it can be said that a refinement in the microstructure of a martensitic steel sample will end up in an increased corrosion rate of the sample. In the steel-making process, grain refinement is often used to increase the strength of the alloy [46], but is here found to be less favourable from corrosion point of view. Previous research on the influence of grain size on the corrosion rate of steel proved the opposite [47]: it was found that that in the heat-affected zone of a weld, the grains were bigger, but the corrosion rate increased. However, it turned out that the microstructures of the bulk and heat-affected zone were no longer comparable due to the growth of other, secondary, phase morphologies. This also caused the change in corrosion rate, during those experiments, to be no longer dependent of grain size alone.

3.3 Prior austenite grain size influence on pitting behaviour

The pitting behaviour of the various martensitic specimens was investigated. After 10, 30 and 60 minutes of immersion in the 3.5wt% NaCl, images of the corroded surface were taken using an optical microscope. In the previous section, it was seen that the surfaces of the martensitic samples were very active, because virtually no passive regime was observed during these polarization experiments. This high activity is expected to influence the pitting behaviour as well: the passive layer will be broken down easily and pits are more likely to form after short submersion times. Previous research [25], also showed the passive region in the polarization curve to become smaller (and vanish eventually) for increasing amounts of martensite.

Figure 3.26 shows the 3 samples after 10 minutes of submersion. Various pits can be observed in the surface, appearing as bright spots on the dark (non-corroded) background. In the caption of the figure the number of pits, on the sample surface, is displayed. It must be mentioned that this number represents pits (or bright spot in the images), with a diameter larger than $50\mu m$, since that was the smallest size that could be detected with the microscope at this magnification. It can be seen that the number of pits was decreasing with decreasing prior austenite grain size.

(a) M2, 41.4μm, 10 min, number of pits: **216**

(b) M3, 22.3μm, 10 min, number of pits: **153**

(c) M4, 8.6μm, 10 min, number of pits: **29**

Figure 3.26: Corroded surfaces of the martensitic samples after 10 minutes of submersion, scale: area size is 8x5mm

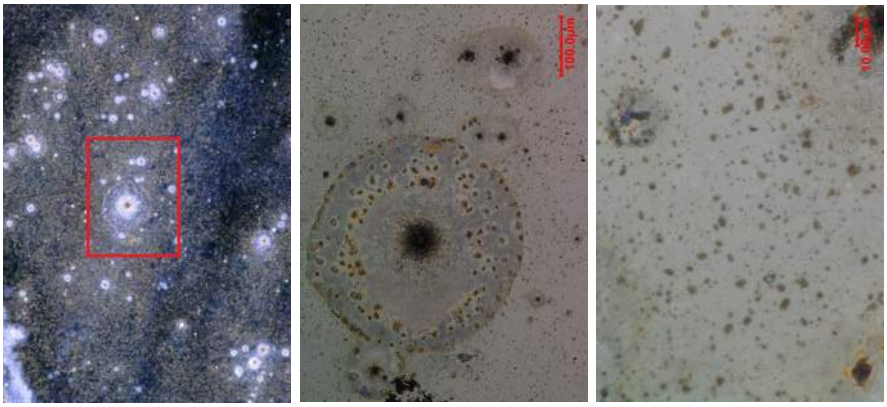

(a) 10 min, 50x (b) 10 min, 500x (c) 10 min, 2500x

Figure 3.27: Zoom-in sequence on the mist around a pit in sample M4 after 10 minutes of submersion

Besides the bright pits in Figure 3.26, a mist was observed, surrounding the pits. To find out what was causing this mist, more close-up images were taken from sample M4, as can be seen in Figure 3.27. In Figure 3.27a, a relatively large pit can be seen, having a diameter of roughly $100\mu m$. Around this pit, the mist is observed as well. When the magnification was increased, up to 2500x as in Figure 3.27c, it can be seen that the mist was made up from many very small pits having sizes of around several micrometers.

Figure 3.28 shows the corroded surfaces after 30 minutes of submersion, together with the number of pits that were larger than $50\mu m$. It can be seen that the amount of pits was increasing with respect to the situation after 10 minutes of submersion, for all 3 samples. The relative increase in number of pits was similar for all 3 samples, being around 25%. It can be seen as well that the mist had started to disappear on the surface of sample M2, while M3 and most certainly M4 still had this mist on the surface.

Figure 3.29 shows the corroded surface after 60 minutes of submersion in the NaCl-solution. The number of pits, larger than $50\mu m$, had increased by roughly 20%. From the images, it also appears that the colour of the pits have changed from white to brown. This can be caused by a change in the (white balance) settings of the camera in the microscope, but could be caused as well by the presence of $Fe(OH)_2$ reaction products on the surface. Especially in Figure 3.29c, for sample M4, a brown ring of reaction

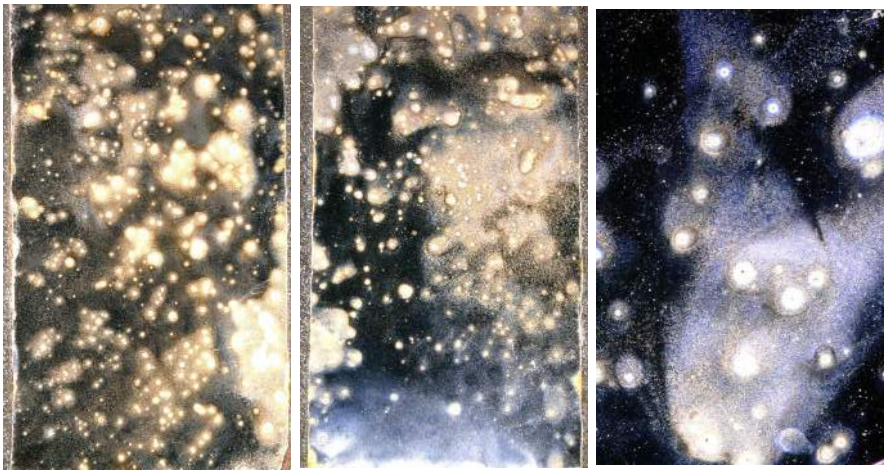

(a) M2, 41.4μm, 30 min, number of pits: **271**

(b) M3, 22.3μm, 30 min, number of pits: **185**

(c) M4, 8.6μm, 30 min, number of pits: **34**

Figure 3.28: Corroded surfaces of the martensitic samples after 30 minutes of submersion, scale: area size is 8x5mm

products was seen around the pit. This ring, in early stage of development, was seen as well around the pit in Figure 3.27b. The mist, composed of small pits, had disappeared for samples M2 and partly for M3. Sample M4 still showed this mist around the pits, while its pits had the largest size as well, up to 400μm in diameter (including the ring of reaction products as in Figure 3.27b).

The number of pits versus time is shown in Figure 3.30. Clearly, the pitting behaviour of the martensitic samples was influenced by the prior austenite grain size. It was seen that the coarse-grained samples have more pits on the corroded surface, while the pits on the fine-grained sample, on the other hand, were larger in size. Previous research [19] also found a fine microstructure to have fewer pits on the corroded surface. This influence of prior austenite grain size is caused by the amount of cathode area that is available to reduce the oxygen. It was found, in the previous section, that increasing the grain boundary density, will make the sample more active. So it follows that grain boundaries form more active sites than to the bulk of the grains. A fine-grained sample has, therefore, more initiation sites for pits. However, as was seen in Section 1.2.3, enough compensating cathode area needs to be present to facilitate the cathode oxygen reduction reaction.

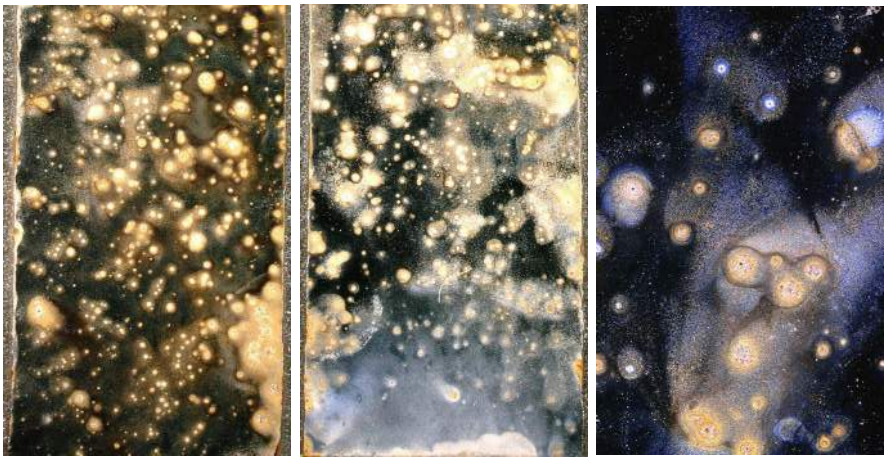

(a) M2, 41.4μm, 60 min, number of pits: **335**

(b) M3, 22.3μm, 60 min, number of pits: **218**

(c) M4, 8.6μm, 60 min, number of pits: **40**

Figure 3.29: Corroded surfaces of the martensitic samples after 60 minutes of submersion, scale: area size is 8x5mm

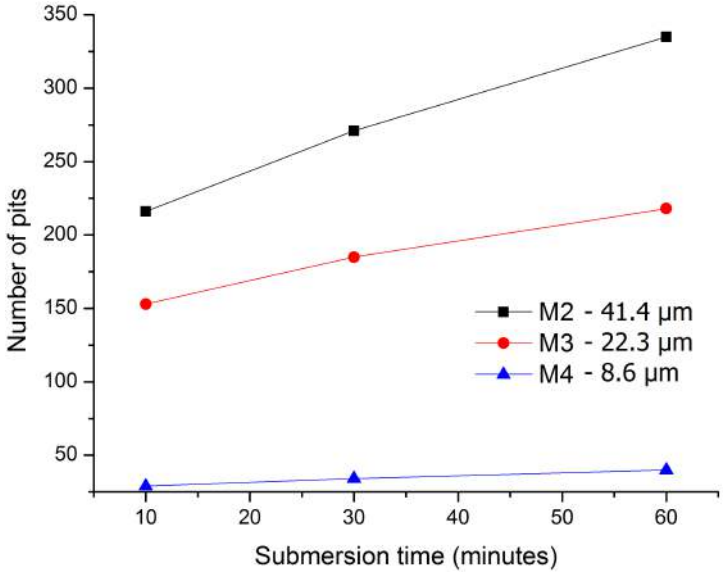

Figure 3.30: Number of pits for martensitic samples after 10, 30 and 60 minutes of submersion

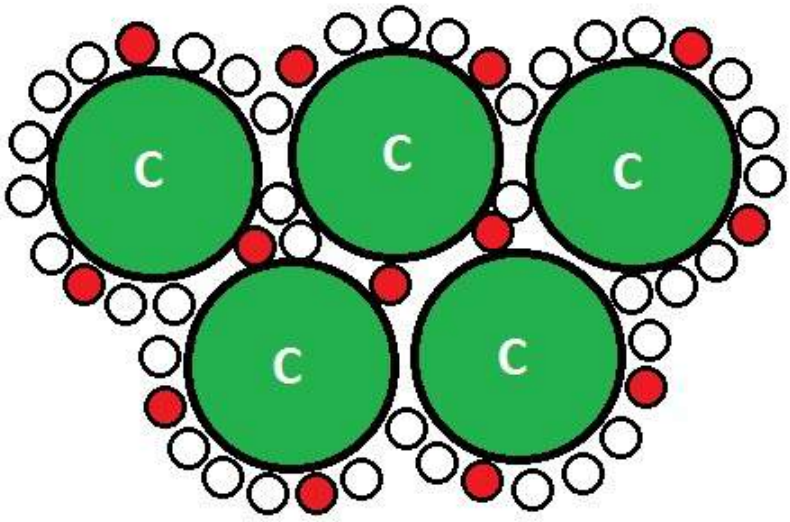

Figure 3.31: Sketch of cathodic ("c") prior austenite grains (green) in a coarse-grained sample, with pit nucleation sites (black circles) on the prior austenite grain boundaries; red circles are initiated pits

Figures 3.31 and 3.32 show a sketch of respectively a coarse- and a fine-grained martensitic sample. The prior austenite grain boundaries were seen as possible initiation sites for pits, represented by the open black circles. The bulk of the (circular) grains was found to be cathodic (shown in green), while the initiated pits are shown in red. It can be seen that in the fine-grained sample, in Figure 3.32, the amount of cathode area was lower per initiation site compared to the coarse-grained sample in Figure 3.31. When the cathode area decreases, the oxygen diffusion towards the cathode will become smaller and the reduction reaction is retarded. This limited amount of oxygen transport is expected to limit the nucleation rate for pits, while the large supply of oxygen to the large cathode area, in the coarse-grained sample, is found to increase the nucleation rate.

It was found in literature that the cathode area, around a pit, will cathodically protect any newly formed pit [4]. This means that in a fine-grained sample, with a large amount of nucleation sites, many initiation sites will become cathodically protected. The pits will start to nucleate up to a small size, but will stop growing from then. This same thing explains the occurrence of the mist on sample M2. It was found that this mist was composed

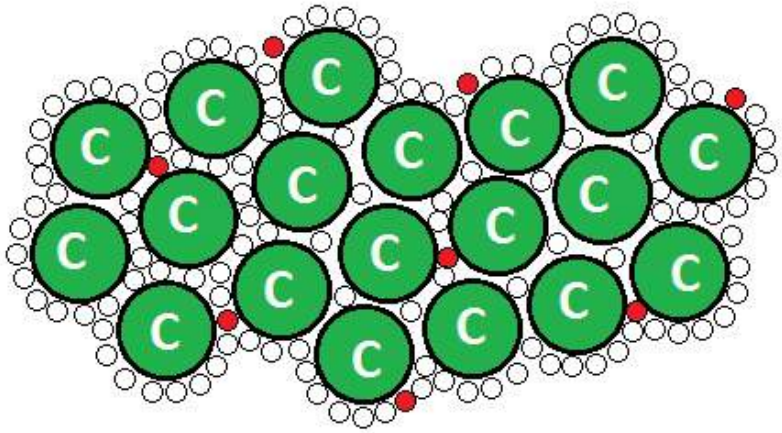

Figure 3.32: Sketch of cathodic ("c") prior austenite grains (green) in a fine-grained sample, with pit nucleation sites (black circles) on the prior austenite grain boundaries; red circles are initiated pits

of many, micrometer-scale pits. Since the mist was present around large pits of more than $50\mu m$ in size, this large pit will cathodically protect the small pits in the mist.

Another factor, contributing to the low amount of pits on the fine-grained samples is repassivation. Repassivation is the process that closes pits again after they have grown to a certain extent [48], of which the process is shown schematically in Figure 3.33. The iron-hydroxide reaction products (displayed in brown) are shown to settle at the sides of the pit, thereby reducing the size of the opening of the pit. This brown ring of reaction products was observed as well in Figure 3.29c. Further growth of this ring will happen when the reaction continues, until the top of the pit will be closed [4]. The pit will then become a closed volume in which, at some point, no more iron can dissolve, since the solution is fully saturated. Repassivation was never reported to be dependent of prior austenite grain size. However, the prior austenite grain size will indirectly change the amount of repassivation, since the amount of present pits did increase with increasing prior austenite grain size.

It has been known that negatively charged chlorine ions are attracted by the positive iron ions. When more pits will close, as a result of repassiva-

tion, a larger amount of chlorine is available per remaining pit, since chlorine is not consumed, but acts as a catalyst. This increase in chlorine content will increase the attack, as the solution in the pits will become more acidic, according to Reaction (1.13). These more harsh environments will increase the penetration depth of the pit in the sample as was the case on sample M4. A proof of this increased penetration depth was the high amount of corrosion products around the pit, which can indeed be seen in Figure 3.29c.

The most dangerous result of pitting is the inward growth of pits. Deep pits can, in pipelines for example, grow through the thickness of pipe walls. These through-thickness pits will then cause leakage of the pipeline. Many shallow pits on the surface are not desired either, but will be less severe since they can be detected better due to the higher amount per unit area. They will also give less mechanical damage, since the majority of the wall thickness of the pipe remains intact.

Summarizing, the corrosion rate was found to be increasing with decreasing grain size (as found in the previous chapter), which is undesired. Additionally, the consequence of the pitting of the martensitic samples was also found to become more severe when the prior austenite grain size was decreased. This causes grain refinement to be an unfavourable measure to increase the strength of a (martensitic) steel, as far as the electrochemical properties are concerned.

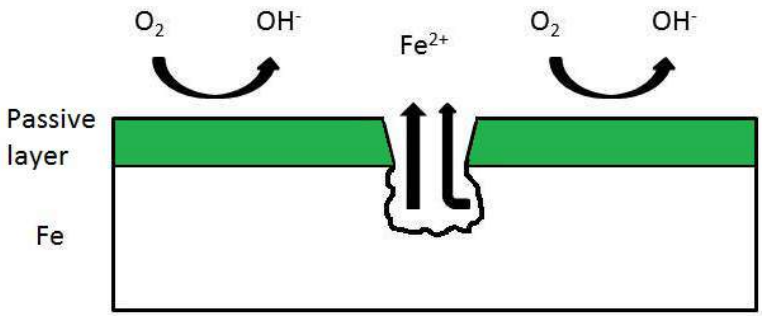

(a) Pit, as a result of local breakdown of the passive layer

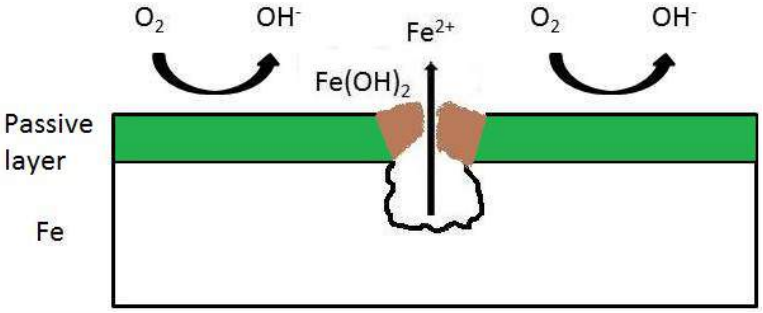

(b) Pit, right before repassivation closes it

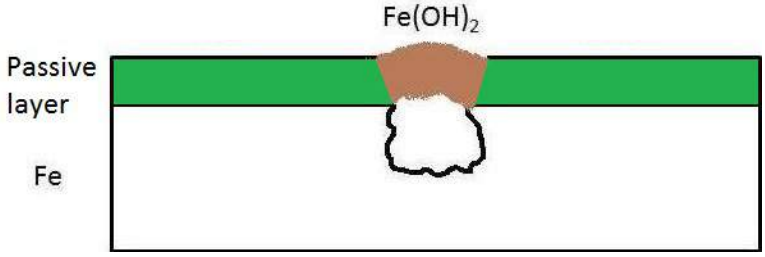

(c) Repassivated (closed) pit

Figure 3.33: Schematic representation of the repassivation mechanism, from top to bottom: iron dissolution in the pit, surrounded by a passive layer (shown in green); accumulation of reaction products (shown in brown) around the pits opening; closure of the pit by iron-hydroxide

3.4 Influence of phase fraction

The influence of phase fraction of the corrosion properties of ferritic-martensitic steel samples has been investigated as well. The samples were polarized in a conventional 3-electrode electrochemical cell, while submerged in a 3.5wt% NaCl solution. The results of the polarization experiments on the dual-phase samples are displayed in Figures 3.34 until 3.37. In these polarization curves, the log current density is displayed versus the applied potential (with respect to the SHE). The corrosion potential of these samples was obtained is a similar way as before with the martensitic samples, as in Section 3.2.

The cathodic branches of the curves, at potentials below the corrosion potential, were very steep: the current density varied little with applied potential due to the lack of oxygen supply to the cathode. In the anodic branches on the other hand, the current density appeared to vary more with applied potential; a sign of a less active surface. The slopes of the anodic branches (and thus kinetics of the iron dissolution) also appeared to change as a result of changing ferrite fractions (between dual-phase samples). Figure 3.38 shows these slopes as a function of the ferrite fraction. The anodic dissolution slope is shown to be increasing for increasing ferrite fraction. Since the slopes in the polarization curves are a measure of reaction kinetics, it can be concluded that the dissolution of iron ions will become more limiting if the ferrite fraction is increased.

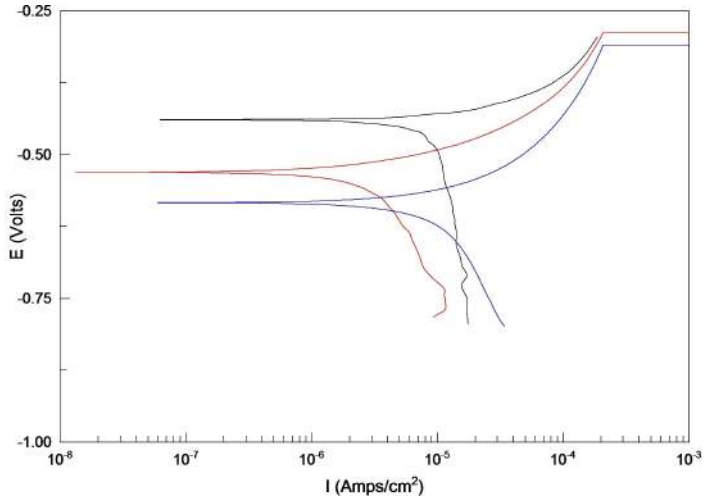

Figure 3.34: Polarization curves for sample DP1, ferrite fraction: 0.526

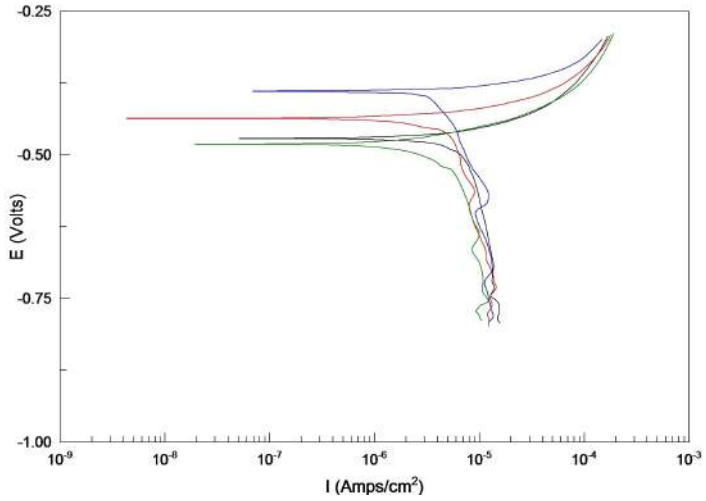

Figure 3.35: Polarization curves for sample DP2, ferrite fraction: 0.445

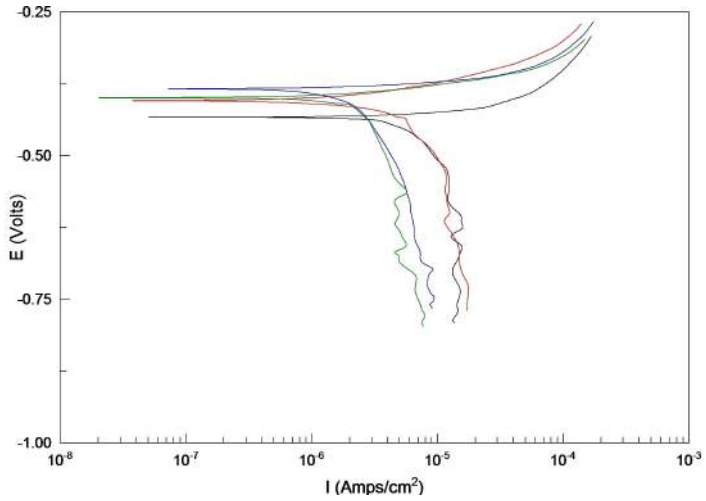

Figure 3.36: Polarization curves for sample DP3, ferrite fraction: 0.336

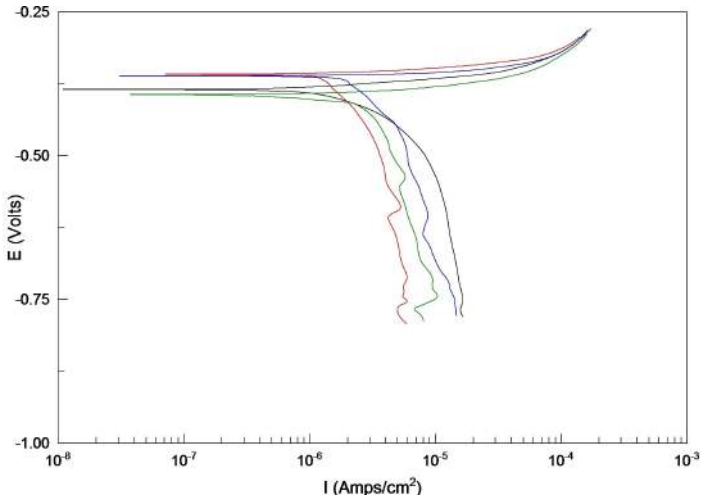

Figure 3.37: Polarization curves for sample DP4, ferrite fraction: 0.146

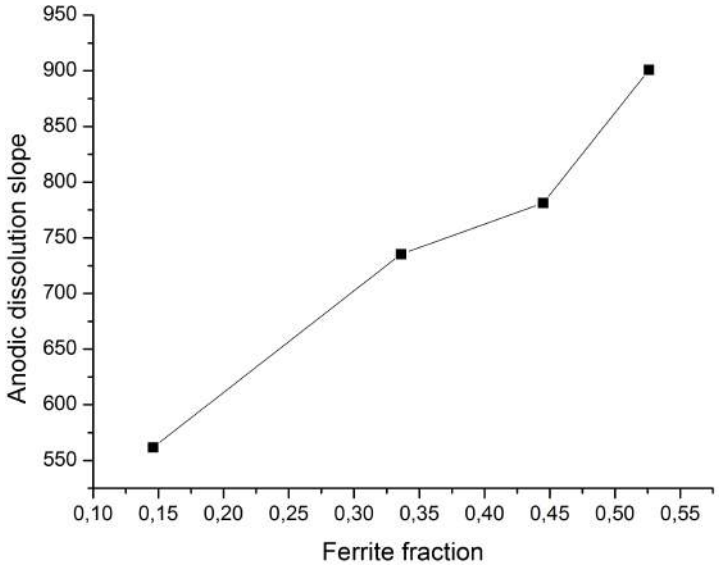

Figure 3.38: Inverse anodic dissolution slopes for dual-phase samples

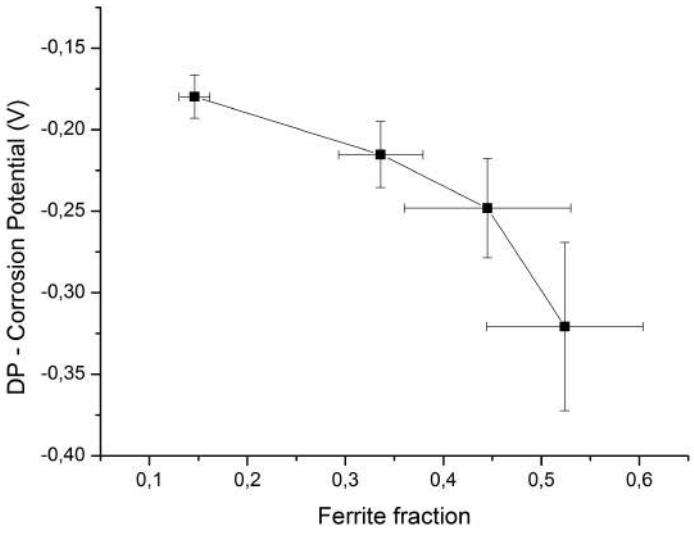

Figure 3.39: Corrosion potential for the ferritic-martensitic samples, showing horizontal error bars for the ferrite fraction and vertical error bars for the measured potential values

Figure 3.39 and Table 3.6 show the measured corrosion potential versus the ferrite fraction for these dual-phase samples. It can be readily seen that the corrosion potential was decreasing to more negative values when the ferrite fraction was increased. It was found before [19] that the corrosion potential of ferrite was lower than the corrosion potential of martensite. It is therefore a logical expectation that when the amount of ferrite is increased, while the martensite fraction decreased, the overall corrosion potential will decrease. A result of introducing ferrite in martensite, with dissimilar corrosion potential, is the formation of a galvanic couple between the ferrite and the martensite, in which ferrite will become the least noble metal.

The corrosion current density of the dual-phase samples is displayed in Figure 3.40 and Table 3.6 versus the ferrite fraction. It can be seen that, with increasing ferrite fraction, the current density first increased but decreased later when the ferrite fraction was larger than 0.336. The increase is caused by the anode in the galvanic couple, ferrite, becoming bigger so more reactive area becomes exposed to the electrolyte. When the ferrite fraction becomes too high, in this case above 0.336, the cathode area fraction, which is equal to the martensite fraction in this case, is too low. This means that the supply of oxygen towards the cathode is too low to consume

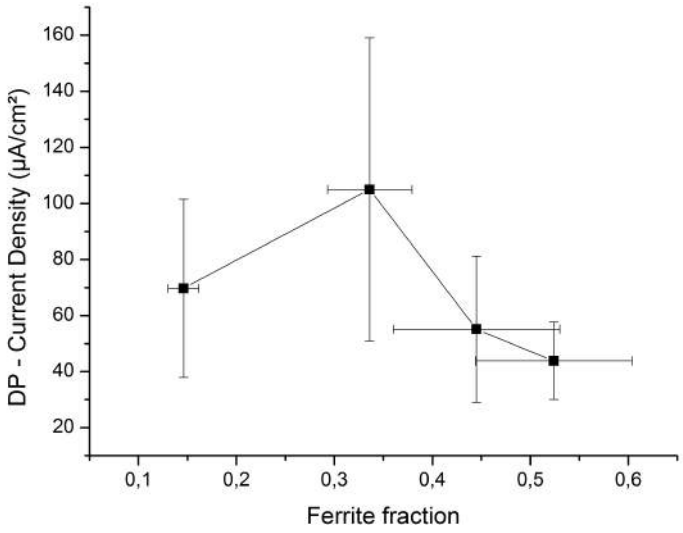

Figure 3.40: Corrosion current density for the ferritic-martensitic samples

all the electrons that were produced at the anode. It must be noted that the error bars for the current density are large, especially for the sample with a ferrite fraction of 0.336. It can be seen in Figure 3.36, that the shape of the polarization curves was similar. However, two measurements are shown to be at a higher current density level, compared to the other two. The measured current was divided by the sample area, which could cause a shift in the current density when the area was measured wrong.

When a galvanic couple is formed, the anodic reaction (in which metal dissolves) only takes place in the anode. Where the current density in Figure 3.40 was calculated for the entire specimen area, it would be more straightforward to calculate the corrosion current for the ferrite alone. Equation

Sample	**Corrosion potential** (mV)	**Current density** $(\mu A/cm^2)$
DP1 - $f_F = 0.526$	-321 ± 51.6	43.8 ± 13.77
DP2 - $f_F = 0.445$	-248 ± 30.4	55.1 ± 26.06
DP3 - $f_F = 0.336$	-215 ± 20.2	105 ± 54.14
DP4 - $f_F = 0.146$	-180 ± 13.3	69.7 ± 31.83

Table 3.6: Corrosion potential and current density of the dual-phase samples

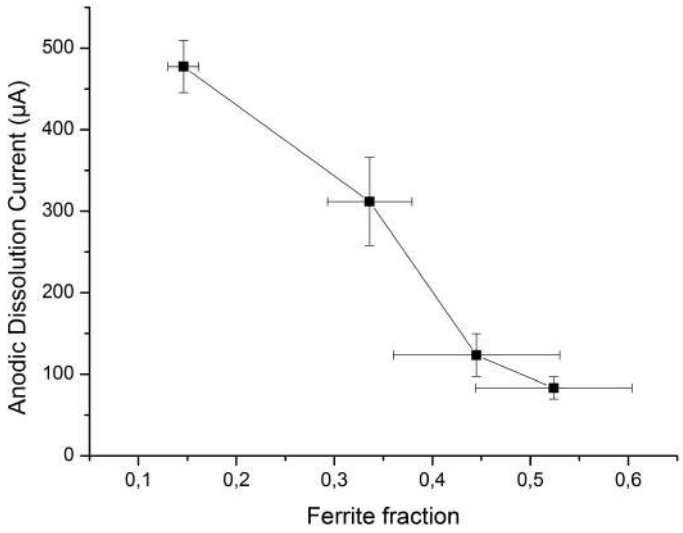

Figure 3.41: Corrosion current for the ferritic-martensitic samples, with the area fraction corrected for ferrite only

(3.1) shows how the corrosion current density is determined from the measured current (I) and sample area (A_{sample}), while Equation (3.2) shows how the current density for the anode alone was calculated taking the ferrite fraction into account.

$$i = \frac{I}{A_{sample}} \tag{3.1}$$

$$i_a = \frac{I}{A_{sample} \times f_F} \tag{3.2}$$

This anodic dissolution current is displayed in Figure 3.41 versus the ferrite fraction. It can be seen that the anodic dissolution current was decreasing with increasing ferrite fraction. This means that the highest corrosion rate, for the anode, was obtained when the ferrite fraction was small. This confirms the presence of a galvanic couple, since the theory (as in Section 1.2.3) predicted the most damaging case for a small anode and a large cathode.

Returning to the increase of the anodic dissolution slopes with ferrite fraction, as was seen in Figure 3.38, this behaviour can be explained further as well now. When the ferrite fraction increased, the cathode area fraction decreased, causing the oxygen reduction reaction to become stagnant. When the cathode reduces less oxygen, fewer electrons are consumed at the

cathode surface. This reduces the kinetics at the anode, because otherwise, an excess of electrons is created that cannot be accommodated. This effect of reduced anode kinetics was indeed observed in Figure 3.38 and the polarization curves. Since the slopes in these polarization curves are a measure for activity, as was already seen for the martensitic samples in Section 3.2, it can be said that the activity of the dual-phase samples reduces with increasing ferrite fractions. This is confirmed by the decreasing anodic dissolution rate, with increasing ferrite fraction.

The obtained results confirm earlier observations on galvanic corrosion; the least noble phase will corrode fastest when its area fraction is low compared to the cathode area fraction. The ferrite was found to be less noble, when coupled to martensite in a microstructure. This has also been reported before [18, 19] when the ferrite was coupled to bainite and martensite. The current research also proved new insights: although the anodic dissolution rate was high in the ferrite alone for low ferrite fractions, the current density (and thus corrosion rate) for the overall sample did show a peak for intermediate ferrite fractions. This means that when the alloy is used in practice, the lowest ferrite fraction will end up corroding less compared to intermediate ferrite fractions. However, the lowest corrosion rate will be obtained when the ferrite fraction is highest (above 0.336).

It must be mentioned that conventional dual-phase ferritic-martensitic steel alloys, that are used in practice rather than in scientific experiments, will have a high ferrite fraction in the order of 80% [49]. When the anode area fraction is this high, the galvanic effect between ferrite and martensite is reduced due to the limited supply of oxygen to the (small) cathode. A change in corrosion rate, as a result of a change in phase fraction for commercial dual-phase alloys, is therefore assumed to be of a smaller extent as compared to what was seen in this section.

3.5 Influence of local composition

The influence of the local composition of the martensite on the corrosion properties has been investigated as well. Using the micro-capillary electrochemical cell, the electrochemical properties of the martensite were investigated by means of polarization of the martensite grains. The goal was to find the dependence of corrosion properties on the local composition. The local composition, unfortunately, was different for each of the alloying elements in the different DP samples, as was seen in Figure 3.16. Therefore, the guiding parameter will be the ferrite fraction of the sample which was, through Figure 3.16, coupled to the composition.

It must be mentioned beforehand that the influence of alloying elements on the corrosion properties of steel has been known for long time. Stainless steels are stainless due to the chromium in the microstructure, that forms a passive chromium-oxide layer on the surface, which impedes further corrosion. The concentrations of elements, like chromium, in the alloy, that is tested here, are however much lower: 0.5wt% instead of roughly 20wt% in commercial stainless steels. The resulting effect on corrosion rate is thus expected to be smaller in these alloys, compared to the effect in stainless steels.

The polarization curves after the polarization of the martensite grains are displayed in Figures 3.42 until 3.45. It can be seen that the curves ap-

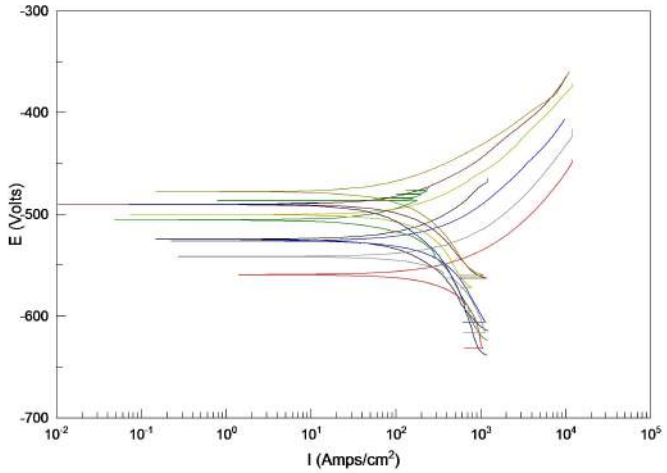

Figure 3.42: Micro-capillary polarization curves, sample DP1, f_F: 0.526

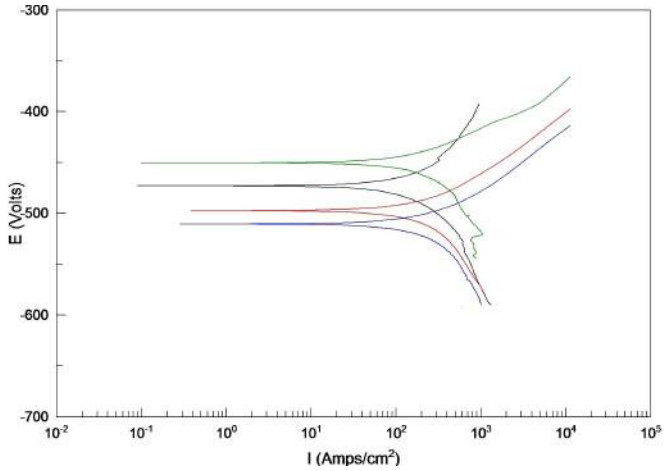

Figure 3.43: Micro-capillary polarization curves, sample DP2, f_F: 0.445

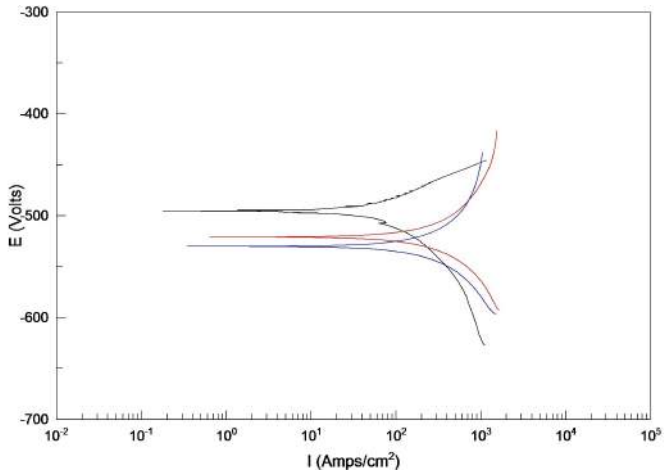

Figure 3.44: Micro-capillary polarization curves, sample DP3, f_F: 0.336

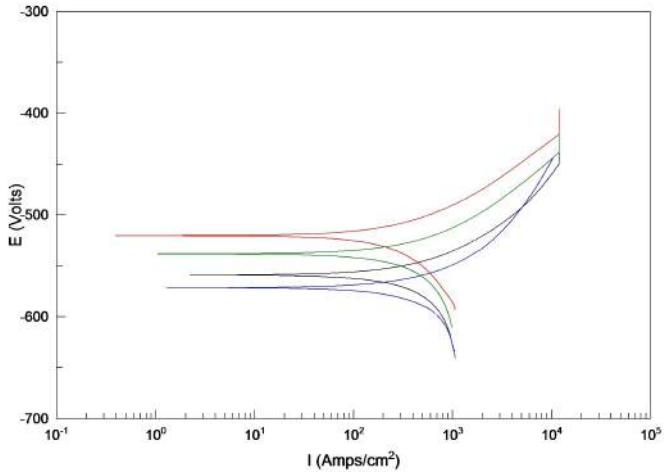

Figure 3.45: Micro-capillary polarization curves, sample DP4, f_F: 0.146

pear to show more scattering than before, after the polarization of the entire sample. This scattering is caused by the practical issues that accompany the usage of the micro-capillary electrochemical cell: the placement of the tip was not similar all the time and the force, with which the tip was pressed onto the surface, varied little, causing the silicone to flex and expose a larger area to the electrolyte.

Figure 3.46 and Table 3.7 show the corrosion potential of the martensite as a function of the ferrite fraction. It can be seen that with increasing ferrite fraction, thus increasing enrichment of alloying elements in the martensite, the corrosion potential increased to more noble values. Only for sample DP1, with the highest amount of enrichment, the potential decreased again. The local composition was thus found to influence the corrosion potential, which is caused by the formation of a galvanic couple between the (metallic) alloying elements and the iron matrix, as was described before by Revie *et al.* [26]. Most alloying elements, except for nickel, were found to have a lower corrosion potential under standard conditions, as was seen in Table 1.2. The more noble iron will become the cathode and the alloying elements will selectively dissolve. The reaction products, such as manganese-oxides, will settle on the surface of the specimen and form a passive layer. This passive layer is expected to decrease the corrosion current density of the sample, since it prevents the iron from getting into contact with the electrolyte. This effect is increased when the ferrite fraction in the sample is

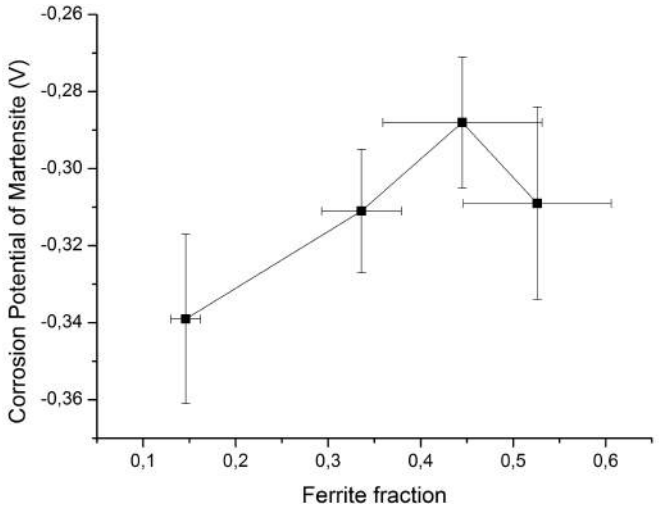

Figure 3.46: Corrosion potential for the martensite in the dual-phase samples using the micro-capillary electrochemical cell

Sample	**Corrosion potential in martensite** (mV)	**Current density in martensite** ($\mu A/cm^2$)
DP1 - $f_F = 0.526$	-309 ± 24.6	0.449 ± 0.3181
DP2 - $f_F = 0.445$	-288 ± 17.0	0.249 ± 0.1511
DP3 - $f_F = 0.336$	-311 ± 16.2	0.334 ± 0.1300
DP4 - $f_F = 0.146$	-339 ± 21.9	0.644 ± 0.3013

Table 3.7: Corrosion properties of the martensite in the dual-phase samples, obtained using the micro-capillary electrochemical cell

increased, since more alloying elements have partitioned into the martensite. As a result, more oxides of alloying elements of elements can settle in the surface, increasing the thickness and rigidity of the passive layer.

Figure 3.47 shows the current density of the martensite for various ferrite fractions. When the martensite was enriched in alloying elements (when the ferrite fraction increased), it was observed that the current density did decrease. This follows the expectation that a passive layer, composed of the reaction products of corroded alloying elements, would lower reaction rate. Sample DP1 shows, just as for the potential, behaviour that was not expected following the other samples, as it showed an increase in current density for increasing amounts of ferrite.

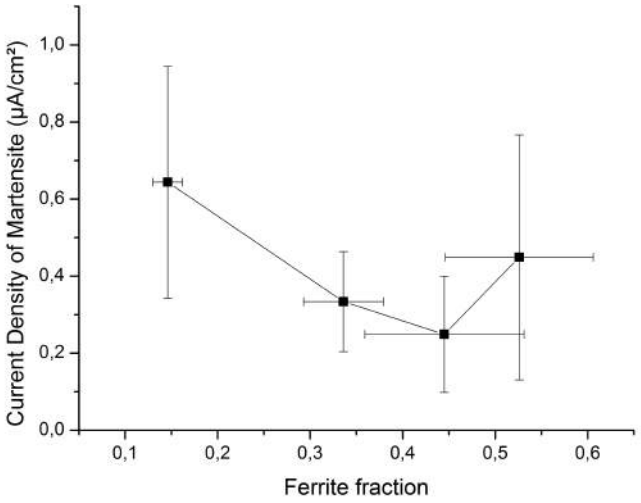

Figure 3.47: Corrosion current density for the martensite in the dual-phase samples using the micro-capillary electrochemical cell

The odd behaviour of sample DP1 is attributed to the high ferrite fraction. It was seen in the optical images (Figure 3.11) that for this sample, the ferrite did not only grow from the prior austenite grain boundaries, but in the bulk of the austenite grains as well. This caused the martensite regions to be less well defined and introduced the risk of placing the capillaries not only in the martensite, but allowed some ferrite to be exposed to the electrolyte as well. A galvanic couple was created by accident, which increased the current density of the sample and lowered the corrosion potential due to the ferrite being less noble than the martensite.

Concluding, it can be said that this experiment did show an influence of local composition on the corrosion properties of martensite. Unfortunately, the influence of the different elements was not found for each of them individually. Previous findings in literature [19, 26] were however replicated, resulting in an increase in corrosion potential for increased amounts of alloying elements. This research, however, had a different approach, since the experiments were done on a micrometer-scale, instead of millimeter-scale. The reduction of the scale caused the changes in electrochemical properties not to be dependent of unwanted variables, such as grain size for example.

3.6 Influence of martensite on corrosion properties in dual-phase steels

In the previous sections, several conclusions have been drawn: a martensitic sample with a higher prior austenite grain boundary density (hence, smaller prior austenite grains) will have a higher corrosion rate. This was caused by the higher (electrochemical) activity of the steel on the prior austenite grain boundaries. This effect has not been observed before in literature, but can be explained by the higher energy level on the prior austenite grain boundaries, as compared to the bulk of the grains.

When a small amount of ferrite is introduced to the martensite, the iron dissolution will take place in the ferrite, due to an occurring galvanic couple, which has been reported in literature before. It was found that the highest iron dissolution rate will occur for very low ferrite fractions, but the corrosion rate on the macroscopic scale will be highest for intermediate ferrite fractions, which was not reported before.

Finally, the introduction of ferrite forces alloying elements into the martensite, which will cause the martensite to become more noble. The extra alloy-

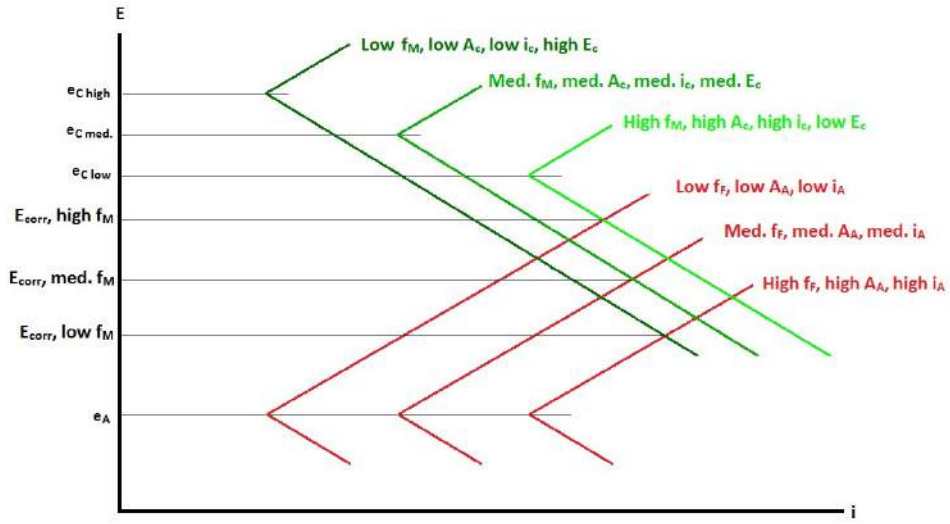

Figure 3.48: Schematic potential versus current density curves for various martensite and ferrite fractions

ing elements selectively dissolved, forming a protective layer of metal-oxides on the iron surface. The corrosion potential of the martensite did increase as a result. This effect has been reported before, and can be compared to the working principle of stainless steels, although the concentrations of alloying elements are lower in this case.

However, this change in electrochemical properties of the martensite, as a function of ferrite fraction, also influenced the overall electrochemical behaviour of the dual-phase samples. The change in electrochemical properties on the macroscopic scale for dual-phase samples, that was seen in Figure 3.39, apparently is not only caused by changing phase fractions, but by changing cathode properties from the martensite as well. This combined effect explains the potential decrease of the dual-phase sample to be progressive with increasing ferrite fraction instead of linear. This can be seen in Figure 3.48 as well, in which a sketch of a polarization curve is displayed. For different phase fractions of ferrite, the cathodic and anodic branches of the polarization curves are shown. The potential of the cathode (martensite) indeed increased with increasing ferrite fractions (due to the enrichment in alloying elements) and the cathodic current density decreased. The anodic dissolution rate is seen to increase with increasing ferrite fraction, just as in Figure 3.41. The resulting exchange corrosion potentials and current densities are seen to follow the measured trends from Figures 3.39 and 3.40.

Chapter 4

Conclusions

During the course of this research, the influence of microstructure on the corrosion properties of ferritic-martensitic dual-phase steel samples has been investigated.

First of all, the prior austenite grain size was varied for martensitic samples. In practice, in the steel-making industry, the grain size is a parameter that is varied as well to change mechanical properties: the steel alloy will generally become stronger when the grain size is reduced. However, this reduction in grain size has been found to be unfavourable as far as electrochemical behaviour is concerned. The grain boundary density is increased when the grain become smaller, meaning that more grain boundaries are present per unit volume. These grain boundaries will have higher energy levels, as compared to the bulk of the grains. This caused the finer-grained martensitic sample to be more active and to have a higher corrosion rate as compared to the coarse-grained sample. It was found as well that when the prior austenite grain size was reduced, the pitting behaviour would deteriorate. The initiation of pits occurred on the grain boundaries (as they were more active) but the compensating cathode area proved to be too small for the growth of all these pits. This resulted therefore in fewer pits for the fine-grained sample, but increased depth of the pits due to higher chlorine concentration in the pits.

The amount of ferrite in the microstructure was also varied for the dual-phase samples. In the steel-making industry, secondary phases are introduced in the microstructure to increase the strength and ductility of the alloy. This research showed that variations in the amount of secondary

phase also influenced the corrosion behaviour of the samples. It was found that ferrite was less noble than martensite, which caused it to sacrificially dissolve once the samples were polarized in the 3.5wt% NaCl solution. The anodic dissolution rate, which is the dissolution rate of Fe^{2+}-ions, was found to be highest for very low ferrite fractions. The overall current density (and thus corrosion rate), however, had a peak at intermediate ferrite fractions of 0.33. Even though the galvanic effect was predicted in literature, it was not expected that the corrosion rate would peak at intermediate ferrite fractions.

The introduction of ferrite also forced higher amounts of alloying elements in the martensite, making it more noble. This increased the potential difference between the ferrite and the martensite even more, increasing the galvanic effect and thereby contributed to an increased corrosion rate.

Concluding, it can be said that several microstructural changes did alter the electrochemical behaviour of the samples. However, the used specimens are different as compared to those that are used in practice. The ferrite fraction in conventional ferritic-martensitic dual-phase alloys is around 80%, resulting in a more favourable cathode to anode area fraction. This decreased the influence of phase fraction and local composition on the corrosion properties of the entire sample. Nevertheless, for future research in metallurgy, these new findings can be implicated to design a steel alloy that will perform well from mechanical point of view, but is also resistant against corrosion without extensive use of coatings or other protection mechanisms.

Chapter 5

Recommendations

During this research project, several conclusions have been drawn on the influence of the microstructure on the corrosion properties of ferritic-martensitic steels. However, some of these findings were obtained by assuming certain processes to be happening or by taking disturbances for granted. In the following section, recommendations are given to verify the assumed theories or to improve the experiments.

- The alumina clamps, that were used in the dilatometer to clamp the samples that were normalized at 1200°C, were found to have undesired behaviour. Their thermal expansion coefficient and thermal conductivity were found to be larger than that of the conventionally used quartz. This resulted in unreliable data for the dilatation of the sample since any occurring expansion could be either caused by the sample or by the clamps. By finding an alternative for the alumina, the dilatation curves for the 1200°C samples will become more useful in the future.

- In the case of the pitting of the martensitic samples, a mist was observed on the surface. It has been observed in the optical microscope that this mist was likely to be caused by very small, just initiated, pits on the surface. For future research, it will be useful to inspect this mist at higher magnifications in the scanning electron microscope (SEM), to verify this conclusion.

- Repassivation was found to occur on the surface of the martensitic samples. This means that pits were closing due to the accumulation of reaction products in the opening of the pit. Using a scanning electron microscope (SEM), this closure can be observed to see if the prior

austenite grain size of the martensitic samples will influence the repassivation process.

- The ferrite was found to selectively corrode when embedded in the martensitic matrix. To verify this, the local thickness reduction of the sample can be measured. This might prove indeed that the ferrite will dissolve sacrificially, while the martensite remains intact. White-light interference [18, 50] could be a useful technique, since it can measure depth profile by analysing the changes in interference of scattered light beams.

- During the annealing in the intercritical regime, alloying elements were partitioned between the ferrite and the austenite. Since the overall concentration of alloying elements in the alloy was higher than the saturation content in ferrite alone, the ferrite was assumed to be saturated with alloying elements. As a result of this, the corrosion properties of ferrite were assumed to be similar in each of the dual-phase samples (with its different ferrite fractions). Future research, for example using the micro-capillary cell, is advised to verify the constant electrochemical behaviour of the ferrite.

- It had not been verified that the micro-capillary measurements on sample DP1 had been performed correctly. The martensite regions have shrunk with respect to the other dual-phase samples; the ferrite was also seen to nucleate in the bulk of the austenite grains instead of at the grain boundaries. When the tips were not placed correctly in martensite alone, ferrite could have influenced the electrochemical properties of the martensite. Therefore, it is advised for the future, to use smaller capillaries to achieve more accurate placement of the tips.

Bibliography

[1] Metals crystal structure. `http://http://www.substech.com/dokuwiki/doku.php?id=metals_crystal_structure/`. Accessed: 2015-03-16.

[2] William D. Callister. *Materials Science And Engineering*. 2010.

[3] Hiromoto Kitahara, Rintaro Ueji, Nobuhiro Tsuji, and Yoritoshi Minamino. Crystallographic features of lath martensite in low-carbon steel. *Acta Materialia*, 54(5):1279 – 1288, 2006.

[4] D.A. Jones. *Principles and Prevention of Corrosion*. Prentice Hall, 2nd edition, 1996.

[5] Qingge Meng, Jun Li, Jian Wang, Zuogui Zhang, and Lixiang Zhang. Effect of water quenching process on microstructure and tensile properties of low alloy cold rolled dual-phase steel. *Materials & Design*, 30(7):2379 – 2385, 2009.

[6] H. Böhni, T. Suter, and A. Schreyer. Micro- and nanotechniques to study localized corrosion. *Electrochimica Acta*, 40(10):1361 – 1368, 1995. 6th International Fischer Symposium on Nanotechniques in Electeochemistry.

[7] David Lide. *CRC handbook of chemistry and physics : a ready-reference book of chemical and phyical data*. CRC Press, Boca Raton, FL, 1990.

[8] A.J. Bard and L.R. Faulkner. *Electrochemical Methods: Fundamentals and Applications*. Wiley, 2000.

[9] National Association of Corrosion Engineers, R. Baboian, and R.S. Treseder. *NACE Corrosion Engineer's Reference Book*. NACE International, 2002.

[10] R.J. Naumann. *Introduction to the physics and chemistry of materials*. CRC Press, 2008.

[11] D.A. Porter and K.E. Easterling. *Phase Transformations in Metals and Alloys, Third Edition (Revised Reprint)*. Taylor & Francis, 1992.

[12] C.Y. Kung and J.J. Rayment. An examination of the validity of existing empirical formulae for the calculation of ms temperature. *Metallurgical Transactions A*, 13(2):328–331, 1982.

[13] H. Bhadeshia and R. Honeycombe. *Steels: Microstructure and Properties: Microstructure and Properties*. Elsevier Science, 2011.

[14] S. Morito, H. Tanaka, R. Konishi, T. Furuhara, and T. Maki. The morphology and crystallography of lath martensite in fe-c alloys. *Acta Materialia*, 51(6):1789 – 1799, 2003.

[15] M. Durand-Charre. *Microstructure of Steels and Cast Irons*. Engineering Materials and Processes. Springer Berlin Heidelberg, 2013.

[16] Basim O. Hasan. Galvanic corrosion of carbon steelbrass couple in chloride containing water and the effect of different parameters. *Journal of Petroleum Science and Engineering*, 124(0):137 – 145, 2014.

[17] B. Díaz, L. Freire, X.R. Nóvoa, and M.C. Pérez. Electrochemical behaviour of high strength steel wires in the presence of chlorides. *Electrochimica Acta*, 54(22):5190 – 5198, 2009. Selection of papers from the 59th Annual Meetingof the International Society of Electrochemistry7-12 September 2008, Seville, Spain.

[18] Shaopeng Qu, Xiaolu Pang, Yanbin Wang, and Kewei Gao. Corrosion behavior of each phase in low carbon microalloyed ferritebainite dual-phase steel: Experiments and modeling. *Corrosion Science*, 75(0):67 – 77, 2013.

[19] Lakshmana Rao Bhagavathi, G.P. Chaudhari, and S.K. Nath. Mechanical and corrosion behavior of plain low carbon dual-phase steels. *Materials & Design*, 32(1):433 – 440, 2011.

[20] P.P. Sarkar, P. Kumar, Manas Kumar Manna, and P.C. Chakraborti. Microstructural influence on the electrochemical corrosion behaviour of dual-phase steels in 3.5 *Materials Letters*, 59(1920):2488 – 2491, 2005.

[21] K.D. Ralston, N. Birbilis, and C.H.J. Davies. Revealing the relationship between grain size and corrosion rate of metals. *Scripta Materialia*, 63(12):1201 – 1204, 2010.

[22] K.D. Ralston and N. Birbilis. Effect of grain size on corrosion: A review. *Corrosion*, 66(7):075005–075005–13, 2010.

[23] A.H. Ramirez, C.H. Ramirez, and I. Costa. Cold rolling effect on the microstructure and pitting resistance of the nbr iso 5832-1 austenitic stainless steel. *International Journal of Electrochemical Science*, 8(12):12801–12815, 2013. cited by 1.

[24] P. Marcus, V. Maurice, and H.-H. Strehblow. Localized corrosion (pitting): A model of passivity breakdown including the role of the oxide layer nanostructure. *Corrosion Science*, 50(9):2698 – 2704, 2008.

[25] Oğuzhan Keleştemur and Servet Yıldız. Effect of various dual-phase heat treatments on the corrosion behavior of reinforcing steel used in the reinforced concrete structures. *Construction and Building Materials*, 23(1):78 – 84, 2009.

[26] R.W. Revie. *Corrosion and Corrosion Control*. Wiley, 2008.

[27] K. Hashimoto, K. Asami, M. Naka, and T. Masumoto. The role of alloying elements in improving the corrosion resistance of amorphous iron base alloys. *Corrosion Science*, 19(7):857 – 867, 1979.

[28] DP600 data sheet TATA Steel. `http://www.tatasteelautomotive.com/static_files/StaticFiles/Automotive/new-2013/Tata%20Steel%20-%20DP600%20CR%20-%20data%20sheet.pdf`. Accessed: 2015-03-31.

[29] David Farias. *Influence of the Microstructure on the Corrosion Performance of DP Steels*. CPI-Koninklijke Wöhrmann, 2014.

[30] M.H Saleh and R Priestner. Retained austenite in dual-phase silicon steels and its effect on mechanical properties. *Journal of Materials Processing Technology*, 113(13):587 – 593, 2001. 5th Asia Pacific conference on Materials processing.

[31] Ali Bayram, Agah Uğuz, and Murat Ula. Effects of microstructure and notches on the mechanical properties of dual-phase steels. *Materials Characterization*, 43(4):259 – 269, 1999.

[32] Applications of dual-phase steel in the automotive industry. http://www.worldautosteel.org/steel-basics/steel-types/dual-phase-dp-steels/. Accessed: 2014-11-10.

[33] Shoujin Sun and Martin Pugh. Properties of thermomechanically processed dual-phase steels containing fibrous martensite. *Materials Science and Engineering: A*, 335(12):298 – 308, 2002.

[34] ASTM E562-08. Standard Test Method for Determining Volume Fraction by Systematic Manual Point Count. 2008.

[35] MacDiarmid Emerging Scientists Association guid on measuring grain size using ImageJ. http://mesa.ac.nz/?page_id=3813. Accessed: 2015-04-01.

[36] Company information about the used dilatometer. http://thermophysical.tainstruments.com/instruments/dilatometers/dil-805ad-quenching-and-deformation-dilatometer/. Accessed: 2015-04-23.

[37] Specifications of the dilatometer in Delft University. http://labs.tudelft.nl/index.php?action=instrument&id=138. Accessed: 2015-04-23.

[38] Engineering toolbox materials database. http://www.engineeringtoolbox.com/linear-expansion-coefficients-d_95.html. Accessed: 2015-03-31.

[39] Achim Walter Hassel, Koji Fushimi, and Masahiro Seo. An agar-based silver—silver chloride reference electrode for use in microelectrochemistry. *Electrochemistry Communications*, 1(5):180 – 183, 1999.

[40] Ag/AgCl reference electrode. http://automotive.arcelormittal.com/europe/products/AHSS/DP/EN. Accessed: 2015-06-22.

[41] T Suter and H Böhni. Microelectrodes for corrosion studies in microsystems. *Electrochimica Acta*, 47(12):191 – 199, 2001.

[42] T. Suter and H. Böhni. Microelectrodes for studies of localized corrosion processes. *Electrochimica Acta*, 43(1920):2843 – 2849, 1998.

[43] Corrosion of metals and alloys – Electrochemical test methods. (ISO 17475), 2010.

[44] S.-J. Lee and Y.-K. Lee. Effect of austenite grain size on martensitic transformation of a low alloy steel. *Materials Science Forum*, 475-479(IV):3169–3172, 2005. cited by 25.

[45] A. García-Junceda, C. Capdevila, F.G. Caballero, and C. García de Andrés. Dependence of martensite start temperature on fine austenite grain size. *Scripta Materialia*, 58(2):134 – 137, 2008.

[46] G.E. Dieter and D. Bacon. *Mechanical Metallurgy*. Materials Science and Engineering Series. McGraw-Hill, 1988.

[47] Sajjad Bordbar, Mostafa Alizadeh, and Sayyed Hojjat Hashemi. Effects of microstructure alteration on corrosion behavior of welded joint in {API} {X70} pipeline steel. *Materials & Design*, 45(0):597 – 604, 2013.

[48] P. Marcus. *Corrosion Mechanisms in Theory and Practice*. Corrosion Technology. Taylor & Francis, 2002.

[49] Süleyman Gündüz. Effect of chemical composition, martensite volume fraction and tempering on tensile behaviour of dual phase steels. *Materials Letters*, 63(27):2381 – 2383, 2009.

[50] Børge Holme and Otto Lunder. Characterisation of pitting corrosion by white light interferometry. *Corrosion Science*, 49(2):391 – 401, 2007.